UNIVERSITÀ DEGLI STUDI DI MODENA E REGGIO EMILIA

PHYSICS and NANOSCIENCES - School of Graduate Studies

Charge transport in Reduced Graphene Oxide Thin Films

Tesi per il conseguimento del titolo di Dottore di Ricerca

Supervisor:
Prof.
MARCO AFFRONTE

Co-supervisor:
Dott.
ANDREA CANDINI

Candidate:
ANNA VIANELLI

XXVII ciclo
Sessione I - 2016

Contents

Introduction

Graphene Oxide (GO) is the oxidized form of graphene, produced by the oxidation of crystal graphite with a mixture of sulfuric acid, sodium nitrate, and potassium permanganate (the Hummers method [1]). Structurally, GO can be visualized as a graphene sheet with its basal plane decorated by oxygen-containing groups. Due to high affinity to water molecules by these groups, GO is hydrophilic and can be dissolved in water. The solubility in water makes the deposition straightforward through easy and cheap methods. GO is a poor conductor but its treatment by light, heat, or chemical reduction can restore most properties of the famed pristine graphene making it very attractive not only as possible way to obtain graphene in large quantity, but also for its peculiar properties in many applications in different fields.
The most exciting advantages of this method are its low-cost and potential scalability. The starting material is simple graphite, and the technique can easily be scaled-up to produce gram quantities (or larger) of chemically derived graphene dispersed in liquids.
Since all these applications will rely on the deep understanding and the consequent ability of tuning of the properties of the GO, this thesis is intended to study in detail the charge transport in the reduced GO (rGO), also in presence of applied magnetic fields.

Chapter One is an introduction of the basic properties of the GO and rGO, in terms of morphological and spectroscopic characterization, and the main literature about charge transport is presented.
Chapter Two gives an overview of the main experimental techniques involved in the realization of this project, including preparation, deposition, reduction

and characterization of the samples.

Chapters Three concerns the detailed study of the reduction process by thermal annealing. The samples are characterized by micro-Raman spectroscopy in order to reveal structural changes due to reduction, and the process is then monitored directly through *in-situ* electrical measurements.

Chapter Four presents the main results on charge carrier transport in rGO thin films. The electrical characterization has been carried out as a function of temperature and applied magnetic fields for samples annealed at different temperatures and the flake size dependence has been investigated.

Finally, chapter Fives presents preliminary results on a GO-based device in vertical spin valve geometry.

At the end is given a general conclusion to the work and some future perspectives on the basis of the obtained results.

Chapter 1

Graphene oxide: fundamentals and properties

The term graphene refers to a class of different materials [2, 3]. The ideal graphene, a two dimensional monolayer of sp^2-bonded carbon atoms arranged in the typical honeycomb hexagonal structure, can be obtained through the mechanical exfoliation of the graphite. This method allows the production of a type of graphene which display unique physical properties as very high electron mobility, high thermal conductivity and excellent optical and mechanical properties.

Besides this method, it is possible to find graphene derived from chemical vapor deposition (CVD), from epitaxial growth on SiC, from molecular assembly or the so called chemically derived graphene, which comes from the exfoliation of graphite in liquid phase.

Each of these methods results in different quality (in terms of defect density) and different amount of graphene, therefore making each method more suitable for a specific application.

While the mechanical exfoliation of graphite is the most reliable method to produce high-quality graphene, its low yield limits the integration in practical applications, relegating it to the research field.

The interest around graphene oxide (GO) spread after the discovery of graphene in 2004 as promising viable route to obtain large area and processable monoatomic-

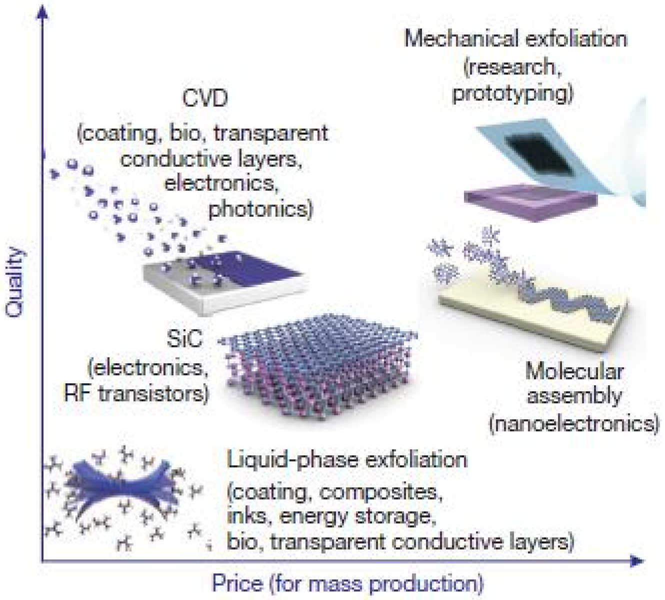

Figure 1.1: Several methods of mass production of graphene. [2]

thick sheets of graphene.

Graphene oxide, anyway, has an history much older and complex than that of graphene: the first well-known study was published back in 1859 by Brodie [4], who was studying the structure and the molecular weight of graphite.

Differently from pristine graphene, GO can be obtained with sheet sizes tunable from >100 μm to <1 μm [5], can be functionalized with different molecular moieties [6] allowing to process it in water or organic solvents [7] and to deposit it on different substrates with a very high monolayer yield [8]. The low production cost, the high solubility and wide processability, the optical transparency, the tunability of electrical and optical properties of GO and the possibility of chemical functionalization, make it suitable for a variety of applications, such as production of paper-like materials [9], conductive electrodes for flexible electronics [8, 10], energy storage [11, 12, 13, 14, 15, 16], optical applications [17] and gas sensing [18, 19, 20] among others.

1.1 Synthesis, structural features and deposition

About 60 years after Brodie's studies, Hummers and Offeman developed an alternative methods to produce the graphite oxide, by reacting natural flake graphite with a mixture of potassium permanganate ($KMnO_4$) and concentrated sulfuric acid (H_2SO_4), achieving similar levels of oxidation [1].

Since then, other groups proposed slightly modified versions of this method, but very little has changed and the so-called modified Hummer's methods are the most widely used way to produce graphite oxide.

The resulting material is a layered structure of stacked graphene oxide sheets that, thanks to the functional groups attached to the surfaces resulting from the oxidizing process, are strongly hydrophilic. The hydrophilic characteristic and the derived oxygen functional groups weaken the interlayer bonding and facilitate the exfoliation of the graphite oxide by sonicating or stirring the water/graphite oxide mixture. The final product is a suspension of monolayer graphene oxide sheets.

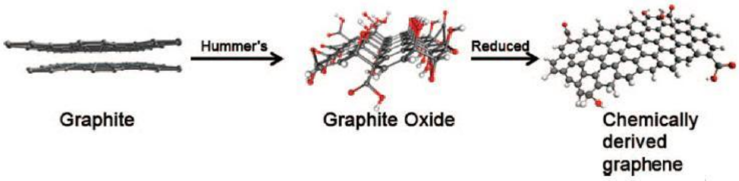

Figure 1.2: Molecular models show the conversion process from graphite to chemically derived graphene. [21]

The most interesting aspect of this method is that it is both scalable and it gives the opportunity of an easy chemical functionalization, hence making GO very promising for a wide range of practical applications.

Generally speaking, GO can be seen as a graphene-like structure where different oxygen-containing functional groups such as carboxyl, carbonyl, hydroxyl and epoxy covalently decorate the surface - either on the basal plane or at the edges -, giving rise to a variable sp^2 and sp^3 hybridized carbon ratio.

Due to its nonstoichiometric atomic composition and to its amorphous nature, there has been a long debate over the years around the structural model for the GO [22]. The prevailing one, the Lerf - Klinowski (LK) model [23], predicts GO to be composed by two different domains that are randomly distributed: intact graphene domains, with sp^2-hybridized carbon atoms, and oxidized domains, which are sp^3-hybridized due to the presence of the aforementioned functional groups (see fig.1.3). These latter domains destroy the long-range conductivity interrupting the conjugation of the graphene-like domains, making GO an electrical insulator.

The graphitic network can be partially restored either by thermal annealing or by exposure to chemical reducing agents, or with a combination of this two methods, but until now it was not possible to completely eliminate the oxygen-containing defects in the carbon lattice. Still, the final products are chemically derived graphene layers of considerable size and exploitable electrical conductivity.

Microscopic investigations of reduced graphene oxide sheets reveal that around the nanometer sized graphene-like islands there are still regions rich of defects, but these are small enough to preserve a sizable electrical conductivity (see section 1.5).

Thanks to its hydrophilic nature, GO is commonly dispersed in water, but it can be also easily dispersed in organic solvents to form colloidal suspensions. This versatility makes it possible to deposit the GO onto any substrate (also

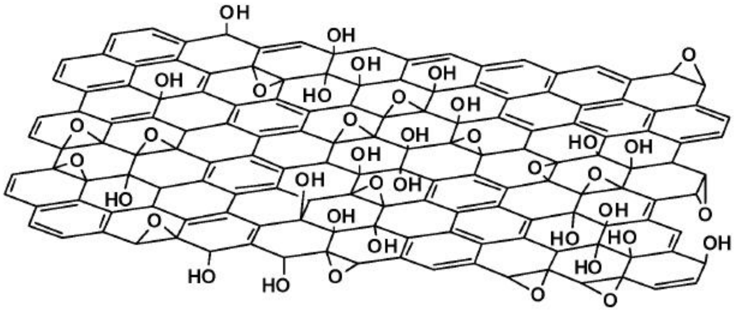

Figure 1.3: Lerf-Klinowski structural model for graphene oxide. [23]

flexible ones) with easy and cheap techniques like drop casting, spin coating, dip coating, spray coating, LangmuirBlodgett (LB) technique and vacuum filtration method.

By employing the LB technique or by spin coating, it is possible to obtain large area homogeneous films, controlling the thickness even down to a single layer, while thicker membranes can be prepared by vacuum filtration or spray coating.

1.2 Morphological characterization

The resulting GO flakes have irregular shapes and can be visualized by optical microscopes, thanks to the contrast created with suitable dielectric substrates, in particular 100 nm or 300 nm SiO_2 on Si [24].

The typical thickness of monolayer GO flakes ranges from 1.0 to 1.4 nm, which is a much higher value than the one observed for pristine graphene, which is usually around 0.5 nm. This is due to the presence of the functionalities which are attached on the basal planes of the flake at both sides.

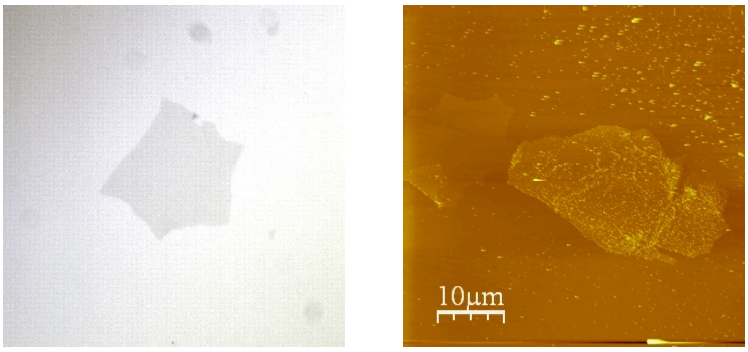

Figure 1.4: Left: Optical image of a single flake graphene oxide on 300 nm SiO_2, magnification 100x. Right: AFM image of a single flake GO and a thicker GO flake.

The average lateral size of the GO flakes can be tuned from few nm to even hundreds of μm by changing the size of the starting graphite and by applying specific protocols during the oxidation procedure.

An easy way to control the flake's dimensions is by changing the time of sonication, which provokes subsequent random fragmentations decreasing the flakes size [25]. The resulting size distribution shows that GO suspensions are characterized by the presence of flakes of different order of magnitude's lateral dimensions, which can be selected only by later centrifugation and filtering procedures [25].

Thin films of GO obtained from solutions with different flake's lateral dimensions also show different morphological characteristics, passing from wrinkled surfaces for larger flakes to very flat films with roughness of about 2 nm for solutions with smaller flakes.

1.3 Reduction techniques

The reduction of GO, i.e. the removal of the oxygen-containing functional groups, partially restores the sp^2 conjugated network allowing the creation of percolating pathways between the intact graphene-like domains, and the material is transformed from an insulator into a graphene-like semimetal [26], although several defects remain in the final graphene lattice (see figure 1.5 and figure 1.6).

The reduction of GO can be achieved via thermal annealing [27, 29], chemical treatments [30] or electrochemical processes [14, 31, 32, 33, 34]. Chemical

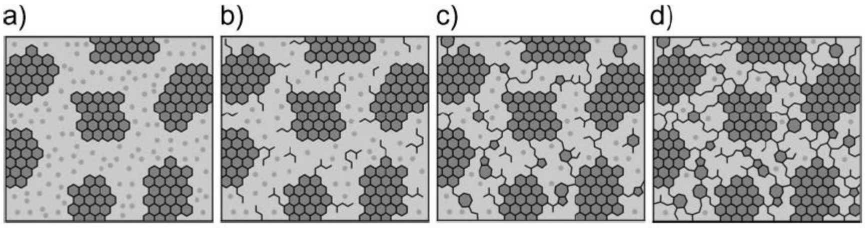

Figure 1.5: Structural model of GO at different stages of reduction by thermal annealing at: a) room temperature; b) ∼100°C; c) ∼220°C; d) ∼500°C. The dark gray areas represent sp^2 carbon clusters and the light gray areas represents sp^3 carbon bonded to oxygen groups (represented by small dots). At 220°C, the percolation among the sp^2 clusters initiates (corresponding to sp^2 fraction of 0.6). The reducing atmosphere used is UHV or Ar/H_2 mixture.[27]

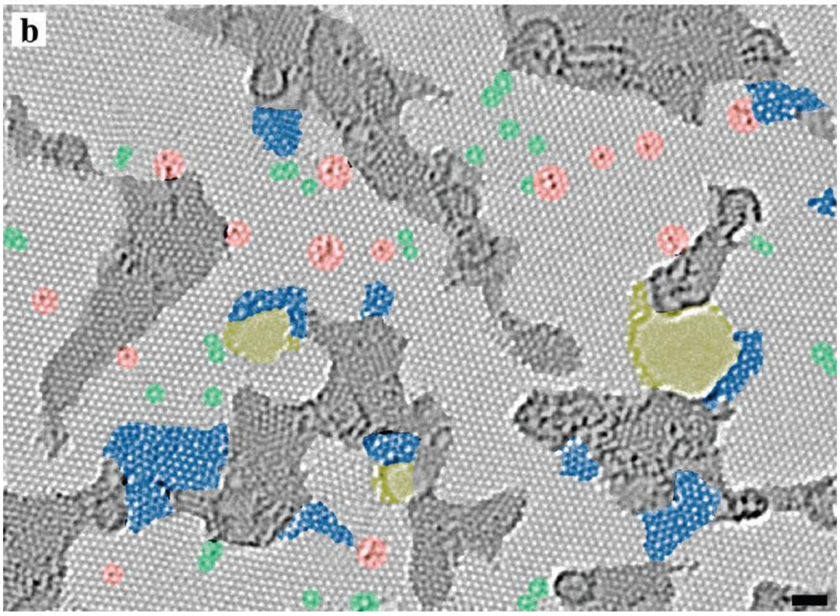

Figure 1.6: Atomic resolution, aberration-corrected TEM image of a single layer reduced-graphene oxide membrane with color added to highlight the different features. The defect free crystalline graphene area is displayed in the original lightgray color. Contaminated regions are shaded in dark gray. Blue regions are the disordered single-layer carbon networks, or extended topological defects, that we identify as remnants of the oxidation-reduction process. Red areas highlight individual ad-atoms or substitutions. Green areas indicate isolated topological defects, that is, single bond rotations or dislocation cores. Holes and their edge reconstructions are colored in yellow. Scale bar 1 nm. [28].

or electrochemical reductions are the most widely used because they can be performed in liquids, producing large amount of rGO with cheap and easy techniques. The drawback is that harmful chemicals are frequently involved, moreover the effect of a specific reagent is selective, preventing the elimination of all the oxygen-containing functional groups.

Thermal mediated reduction, instead, is more effective and thanks to the high temperatures can heal the structural defects through graphitization. On the other hand it has been proved that the rapid increase of temperature provokes the release of CO and CO_2 gases at high pressure [22, 26], which damages the structure of the rGO and creates morphological defects. Usually, an interplay of these two processes occurs, limiting the final efficiency of the thermal annealing.

All these methods lead to a final rGO with varying degrees of reduction in terms of electrical and morphological properties.

1.4 Spectroscopic characterization

Raman spectroscopy is one of the most powerful techniques used to characterize chemically and structurally thin films, since it is non-destructive, fast and with high resolution: for this reasons it became a standard tool also in the investigation of graphene sheets and related materials [35] such as graphene oxide.

Figure 1.7 shows typical Raman spectra of monolayer, bilayer and trilayer graphene oxide samples annealed at different temperatures: they are characterized by two distinct and broad peaks at around 1350 and 1580 cm^{-1} which correspond respectively to the D and the G bands.

The G peak is originated by the primary vibrational mode of graphite and thus of graphene too. In particular it is due to the in-plane vibrational mode involving sp^2-hybridized carbon atoms which compose the graphene lattice. In graphene oxide the G peak is slightly shifted and broader compared to the one of pristine graphene, due to the breakdown of the continuous hexagonal honeycomb graphene lattice [36].

The D peak at ≈ 1350 cm^{-1}, instead, is associated with defects and disorder. It represents a ring breathing mode from sp^2 carbon rings that are located adjacent to a graphene edge or a defect, and it is then a measure of the sp^3-bonding density in the structure [37]. In graphite and pristine graphene, which are ideally free of defects, this peak is very weak or it does not appear at all.

There have been many attempts to exploit Raman spectroscopy in order to characterize the reduction of GO into rGO.

Different groups reports different signals in Raman spectra of GO which they relate to fingerprints of reduction process, as splitting of G peak into G and D' peaks [36, 38], red shift of G peak [39], and the more documented increase

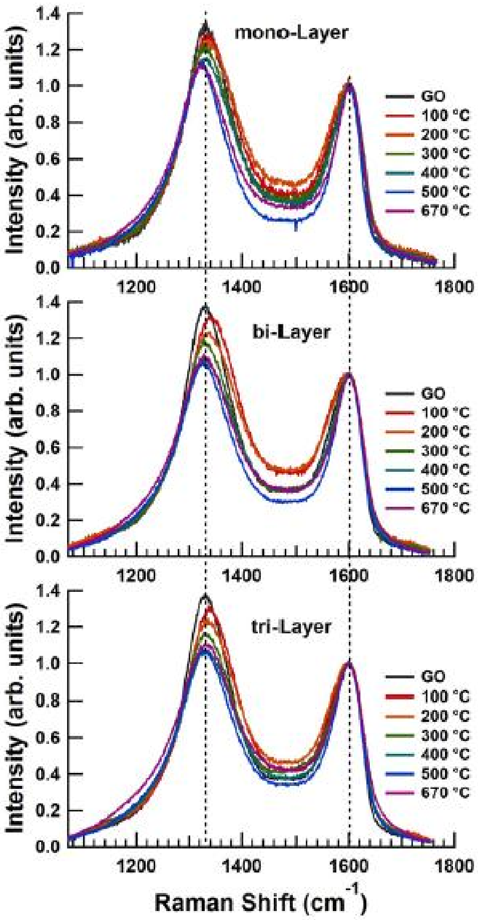

Figure 1.7: Raman spectra of mono-, bi-, and tri-layer GO reduced in UHV at different temperatures, [29].

of the I(D)/I(G) ratio [36, 38, 40] and decrease of full width at half-maximum (FWHM) of the D peak [36, 27, 38].

Yet, some of these observed signals are still quite debated in the literature: for example in references [27, 40] the authors report that the I(D)/I(G) ratio remains constant upon reduction.

It is noteworthy to point out that it is somewhat difficult to compare results reported in the literature, because Raman spectra are usually recorded from samples of various sizes and thickness, therefore making it difficult to make quantitatively comparisons.

Still, some quantitative structural information can be extracted from the micro-Raman spectra. The most used method is to relate the I(D)/I(G) ratio with the lateral size of the graphitic domains L_a, through the empirical Tunistra-Koening equation [41]:

$$\frac{I_D}{I_G} = \frac{C(\lambda)}{L_a} \tag{1.1}$$

where $C(\lambda)$ is the specific constant related to the laser wavelength λ, typically finding values for L_a of few nanometers (from $\sim$ 2 nm [27] to $\sim$ 6 nm [21]).

To study the chemical composition of GO and rGO, X-ray photoelectron spectroscopy (XPS) is the most common spectroscopic technique used because it is particularly suitable in the characterization of surfaces and thin films.

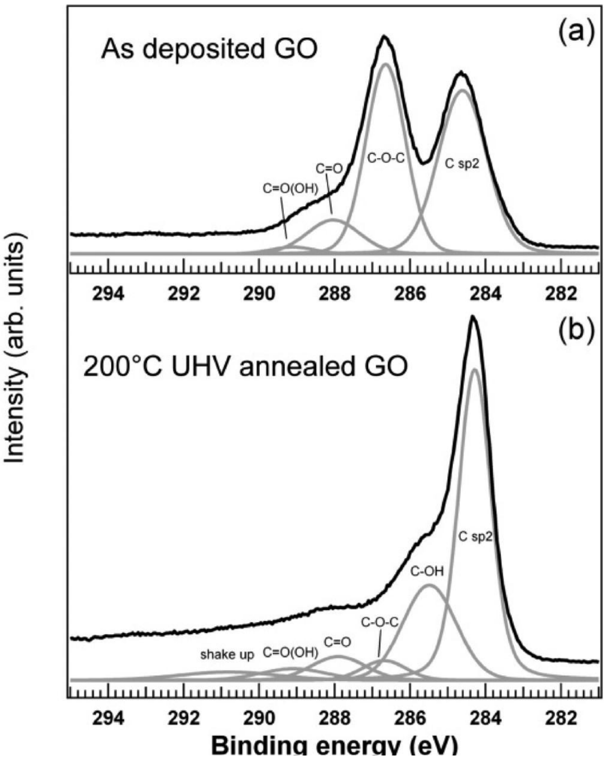

Figure 1.8: XPS C1s core level spectra of as deposited GO (a) and 200°C UHV annealed GO (b), [20].

Through XPS analysis it is in fact possible to measure the carbon-oxygen ratio and to identify the functional groups attached to the surface, by the deconvolution of the C 1s and the O 1s core level spectra in different contributions, each representing one single functional group.

Figure 1.8 shows a typical result of the reduction by annealing of the GO: the peaks are usually fitted as the sum of 5 components, i.e. the sp^2-hybridized carbon, the hydrogenated carbon (C=C / C-C or C-H), hydroxyl groups and epoxy groups (C-OH and C-O-C), carbonyl groups (C=O) and carboxyl groups (C=O(OH)).

The reduction results in a clear decrease of those groups which contain oxygen, and a sharp increase of the aromatic rings peak, indicating a general loss of oxygen alongside a restoration of the sp^2 carbon domains.

Figure 1.9 shows the relative abundance of these groups by increasing annealing temperature [29] and in the inset it is possible to see the calculated C/O ratio, which passes from 2.0 to 8.0 monotonically as the temperature increases. Higher C/O ratio are reported for higher annealing temperature, for instance in ref. [40] where a C/O ratio of 14.1 is found for UHV heat treatment at 900°C.

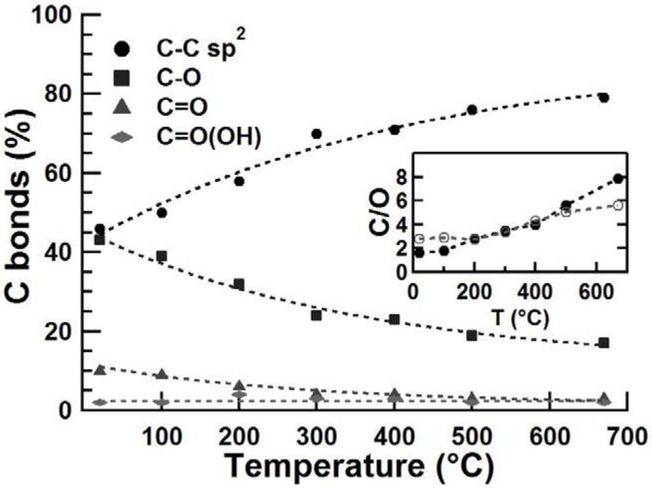

Figure 1.9: Relative abundances of the functional groups in GO as a function of the UHV annealing temperature. Inset: C/O ratio obtained, respectively, from the integrated intensity of C 1s and O 1s spectra (full circles) and from the stoichiometric analysis of the C 1s components (open circles), [29].

1.5 Transport properties of GO and rGO

Despite a huge number of publications focusing on the applications of GO in diverse fields, a full control of charge transport has not been achieved and more systematic studies could widen the GO potentials for electronics.

As discussed above, the as-synthesized GO is an electrical insulator due to the presence of the functional groups which break the conjugated structure and localizes π-electrons. Even though graphitic domains are present, there are no pathways for electrons to move from one to another, but as soon as the sp^2 conjugation is restored with the reduction processes, electrical conductivity is recovered.

Usually the electric transport in reduced graphene oxide is described within a variable range hopping (VRH) model, characterized by:

$$R(T) = R_0 \exp\left(\frac{T_0}{T}\right)^p \tag{1.2}$$

where R_0 is a prefactor, T_0 is a characteristic temperature and p is a characteristic exponent, the value of which distinguishes different conduction mechanism.

In particular, for Mott type of variable range hopping, p is equal to $p = 1/(D+1)$, with D being the dimensionality of the system [42], and thus results to be equal to 1/3 for 2D Mott-VRH or to 1/4 for 3D Mott-VRH. Otherwise, it can assume the values of 1/2 for 2D Efros-Shklovskii VRH or 1 for thermally activated Arrhenius-like transport mechanism.

From the paper of Gomez-Navarro et al. [43] who first suggested 2D Mott VRH as the dominant charge transport mechanism down to around 80 K in individual chemically reduced GO flakes (see figure 1.10), a number of other groups reported similar results [44, 45, 46, 47].

However, also deviations from Mott-VRH model are observed at high temperatures, ascribed to a crossover to an Arrhenius-like regime [45], while electric-field-driven tunneling has been proposed as the dominant mechanism at very low temperatures and high electric fields [44]. Wang et al. [48], found that the transport is governed by two different Arrhenius equations in the high- and low-temperature regime, while Joung and Khondaker [49] proposed 2D Efros-Shklovskii VRH as the dominant transport mechanism in their rGO films.

All these studies were limited in temperature and in the level of GO reduction, thus a fragmented scenario appears from the literature.

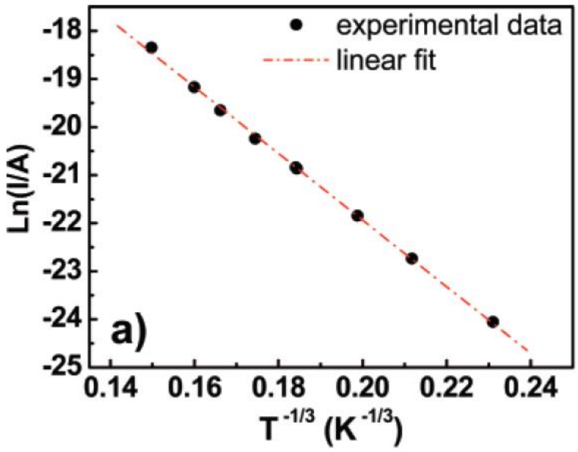

Figure 1.10: Semilogarithmic plot of current I versus $T^{-1/3}$ of a chemically reduced GO monolayer (Vbias = 0.2 V). [43]

Another interesting scientific challenge is to understand the magnetic properties of GO. Only few papers concern the electrical transport of rGO under an applied magnetic field. Zhou et al. [50] reported a change from positive to negative magnetoresistance in pristine graphene where disorder was introduced gradually. In very disordered samples they observed a significant non-saturating negative magnetoresistance up to several percents.

Wang et al. [48] and Muchharla et al. [47] reported negative magnetoresistance of much lower intensities in chemically reduced graphene oxide films.

This thesis contains a systematic study of the electrical properties of thermally reduced GO films, which were prepared at several reduction levels in a controllable way, i.e. by changing the annealing temperature. It has been possible to achieve distinct resistive states of rGO, which allow to control rGO electrical characteristics through a simple fabrication protocol. Also

the dependence on an applied magnetic field of the resistance has been investigated, finding very high non-saturating negative magnetoresistance values at low temperature.
All this results will be presented in chapter 4.

Chapter 2

Experimental methods

2.1 GO preparation

Graphene oxide was prepared using a modified Hummers method starting from graphite flakes (maximum particle diameter 500 μm) by the group of V. Palermo at the ISOF Institute of the CNR of Bologna [5].

Graphite (5g) and 3.8 g of $NaNO_3$ was introduced in a 2 L flask equipped with a mechanical stirring apparatus. Then, H_2SO_4 (375 ml) was added at 0°C (ice bath), and the solution was stirred until it became homogeneous. $KMnO_4$ (25 g) was slowly added over 1 h, keeping the temperature below 10°C with an ice bath. The solution was removed from the ice bath after 2 hours, and was further stirred for 5 days at room temperature (color change from dark green to brown). 700 ml of H_2SO_4 5% aqueous solution were added to the brown suspension dropwise (temp. $<40°C$) and the mixture was stirred for 2 h at room temperature. Then, 20 ml of H_2O_2 (30%) were added drop-wise to destroy the excess of permanganate, and stirred for 2 h. The solution was diluted to 2 L with 5% H_2SO_4 and, after one day of sedimentation, 1 L of supernatant was removed and replaced with water (1 L) and H_2O_2 (10 ml). After vigorous shaking, the suspension was left to sediment overnight.

The supernatant solution was removed and the solid washed with an aqueous mixture of 5 wt% H_2SO_4 and 0,3% H_2O_2 (12 times), then HCl 4% (3 times), milliQ water (10 times) and centrifuged after each step. Finally, the GO was transferred to acetone and dried at 60°C.

The GO powder was then dissolved in water (4 mg/mL), thoroughly stirred for 24 h, and centrifuged to remove aggregates.

All the chemicals were provided by Sigma-Aldrich, and the water used was ultrapure.

2.2 GO deposition

The deposition of the prepared GO suspensions on different substrates was carried out by simple spin coating method. After some tests, commercially available silicon wafer with nominally 300 nm of silicon dioxide insulating layer was chosen as the most suitable substrate to obtain homogeneous thin films.

The Si/SiO$_2$ substrates have been plasma cleaned for at least few minutes using oxygen as gas (Diener Electronic, Femto Plasma System) with the purpose of cleaning the surface and change the hydrophobicity of the SiO$_2$ surface promoting the deposition of the GO/water solution.

The deposition of GO on the substrate is made by the spin coating method readly after the plasma treatments, at 2000 rpm for 60 s, with around 100 μl/cm^2 of material (SPS Spincoater SPIN150-v3). In order to have an homogeneous film, the spin coating process is repeated twice for each sample. Then the obtained GO films are left to dry under ambient conditions.

This recipe gives a film thickness of $\sim$5 nm for each deposition, so the final thickness of the analyzed samples is $\sim$10 nm.

2.3 GO thermal reduction

One of the most attractive properties of graphene oxide is that it can be reduced to graphene-like conjugated structure by removing the oxygen-containing groups attached to the surface.

Among all the reduction methods present in literature (see chapter 1), we chose to use the thermal annealing: for *in-situ* measurements, thermal treatments are performed in an inert atmosphere (argon), while for other characterizations it was done in high vacuum. The two setup are presented in details in what follows.

2.3.1 Thermal annealing in Argon flow

Thermal annealing in argon flow has been carried out as follows.
The sample was placed on a homemade mica sample holder and contacted for the *in-situ* 2-points resistance measurements with steel spring clips.
For thermal treatments, a Thermo Scientific Lindberg Blue Tube Furnace (Tmax=1500°C) has been used, driven by an integrated Eurotherm temperature controller.

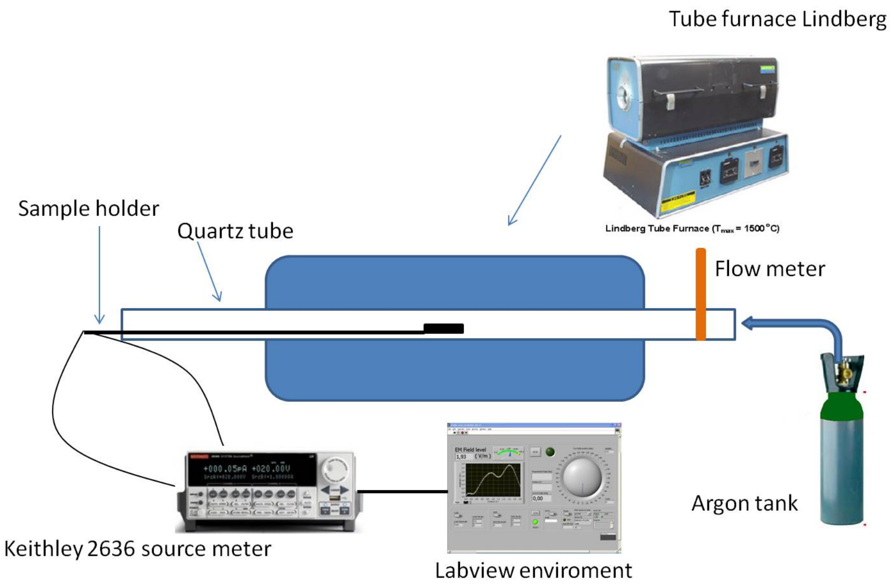

Figure 2.1: Experimental set-up for thermal annealing in argon flow and in-situ resistance measurements.

First, the Argon flow was turned on and controlled by a flowmeter. Then the samples were pushed manually through a quartz tube into the tube furnace, which was preheated at the desired temperature.

Treatments temperatures were 300°C, 400°C, 500°C and 600°C, and the duration of the treatments ranged between 50 minutes and 21 hours.

At the end of the treatment, the sample holder was pulled out from the tube furnace and the sample was allowed to cool at room temperature in argon flow.

The sample holder is connected to a Keithley 2636 source meter through a low-noise triaxial cable. The source meter is then connected to a PC through GPIB cable and interfaced to the computer with a Labview software which I specifically developed for the acquisition of the *in-situ* resistance measurements.

2.3.2 Thermal annealing in high vacuum

Thermal annealing for electrical characterization of reduced GO films has been carried out in a tube furnace in high vacuum ($2{\cdot}10^{-5}/10^{-6}$ mbar) at temperatures ranging between 200°C and 940°C for 1 hour.

For this set of samples, the electrodes are evaporated after the thermal annealing in order to avoid gold contaminations due to diffusion promoted by the high temperatures.

The setup for thermal annealing in high vacuum was developed by Dr. R. Tonini at the FIM Department of the University of Modena and Reggio Emilia (figure 2.2): a quartz tube connects a part in which the sample is introduced and where the vacuum pump system is, with a Thermo Scientific Lindberg Blue Tube Furnace driven by an integrated Eurotherm temperature controller.

As for the thermal annealing in argon flow, samples were pushed manually through the quartz tube thanks to an external magnet into the tube furnace, which was preheated at the desired temperature.

At the end of the treatment, samples are pull out the tube furnace and allowed to cool naturally in vacuum.

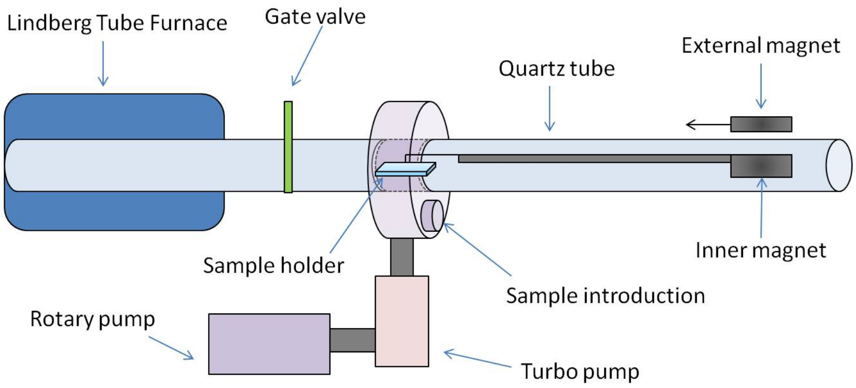

Figure 2.2: Experimental set-up for thermal annealing in high vacuum.

2.4 Devices Fabrication

2.4.1 Electron beam lithography

Some of the measured devices have been fabricated using electron beam lithography.

Electron beam lithography (EBL) is a fundamental technique for mask-less nanofabrication. The working principle is similar to the one of optical lithography: a source of electrons is directed toward a specific sensitive material (resist) in order to impress it. Afterward, with some adequate chemical treatments (development) it is possible to selectively remove or leave intact (negative resists) only the exposed area, enabling the patterning of very small structures, even down to nanometer sizes.

The primary advantage of electron beam lithography is that it allows the patterning of arbitrary custom structures with very high resolution, due to the high focusing of the electron beam.

The quality of the final result will depend on the optics (i.e. the possibility to achieve a highly focused spot), the beam energy, the choice of the resist, substrate and developer and finally the process conditions such as development time and temperature.

Another very important parameter to tune is the area dose, which is related to the beam current I, the time t and the step size S with the following relation:

$$AreaDose = \frac{I \cdot t}{S^2} \tag{2.1}$$

The time t represents the time that an electron takes to penetrate the resist, while the step size S governs the motion of the beam from one position to the next one.

E-beam lithography setup

The electron beam lithography setup used during this PhD work is located at the FIM Department in Modena and consists of Σigma Zeiss SEM connected to a Raith pattern generator..

In figure 2.3 is sketched a typical setup for the electron beam lithography.

The electron beam is produced by thermal field emission from a filament, which ensures stability and high brightness. The created beam is accelerated by a potential difference with values ranging from 0.2 kV to 30 kV. It is possible to choose the beam aperture by a metallic disk placed at the end of the acceleration stage, which has different holes with diameters ranging

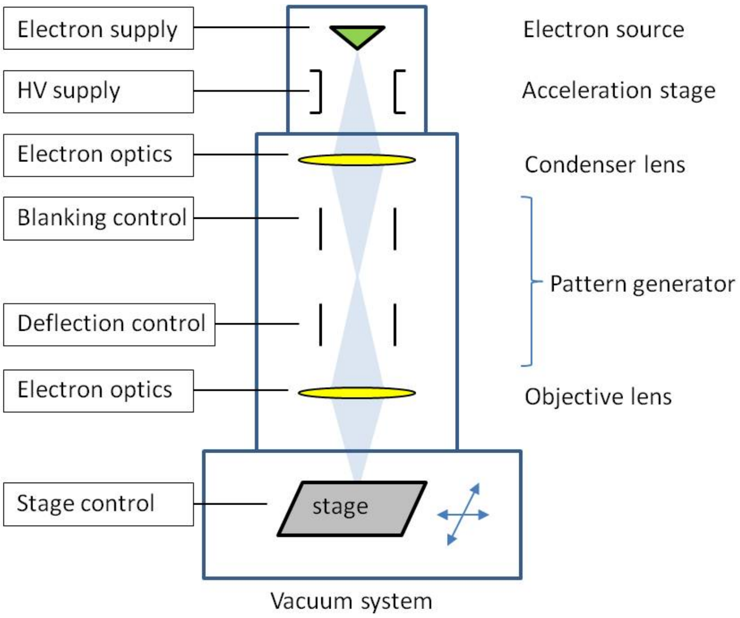

Figure 2.3: Scheme of the setup for the electron beam lithography.

from 7.5 μm to 120 μm, thus selecting the magnitude of the current that will reach the sample (from $\sim$ 15 pA to $\sim$ 5 nA).

Into the column, the beam passes through lenses and plates. The beam blanker is usually made of electrostatic plates which allow one to switch on and off the beam current, so that only the desired area will be exposed to create the final pattern. Then a series of objective lenses permit the focusing of the beam and the correction of defects such as astigmatism.

Finally, at the bottom of the column, there is a deflector which makes it possible to scan the beam across the surface of the sample.

Lithographic process

The different steps of the lithographic process are illustrated in fig. 2.4.

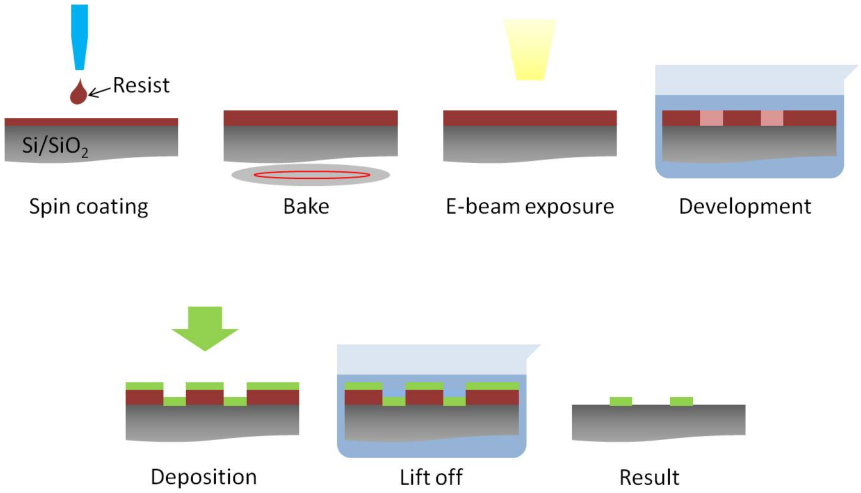

Figure 2.4: Illustration of the lithographic process.

A silicon wafer with a nominally 300 nm thick thermally grown silicon dioxide layer was used as substrate. After cleaning the surface with acetone and sonication, the wafer is covered with a layer of poly(methyl-methacrylate) (PMMA) 4% by spin coating deposition. PMMA is a versatile polymeric material which is widely used as positive resist in nanofabrication with EBL. The covered wafer is then baked on a hot plate: this step is necessary to completely remove the solvent and to convert the polymer into pre-coss-linked resist. Then, the electron beam exposes the resist, breaking the long chain polymers into smaller more soluble fragments. After the exposure, the sample is immersed in a liquid developer. We used for the purpose methyl-isobutyl-ketone (MIBK), which dissolved the areas exposed to the beam. Temperature and duration of the development are very important for the final resolution of the pattern. The development is stopped by the immersion of the wafer in isopropanol (IPA) for a few minutes. The next step is the deposition of the desired material (in this work either GO or Cr/Au for the metalization of the electrodes), followed by the lift-off, which removes all the remaining resist and the exceeding deposited material. This last step is carried out by leaving the wafer into hot acetone (40°C or 50°C) for sufficiently long.

2.4.2 Metal evaporation

For the metalization of the electrodes, the thermal evaporation method was used.

With this technique, a metal is heated up to its melting point in high vacuum atmosphere, so that it starts to evaporate. The metal vapor travels in the vacuum until it reaches a cold surface where it condenses.

The source metal is placed into a boat, usually made of tungsten or another high melting point metal. The boat is connected to two electrodes and a high current is run through it, so that is heats up. Alternatively, if the source metal is in the shape of grains, they can be accommodated into a tungsten basket. Again, the current running through the coil heats up the metal inside, allowing the evaporation (figure 2.5).

The evaporation chamber used during this thesis work hosts two sources

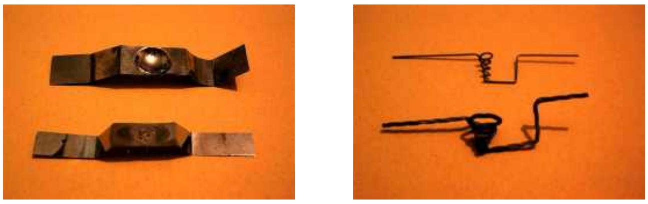

Figure 2.5: Tungsten boats (left) and baskets (right) used for thermal evaporation of Au and Cr respectively.

placements: one has been used with tungsten baskets to evaporate Cr while the other has been used with tungsten boats to evaporate Au. The Cr layer (typically 10 nm) is used as an adhesion layer for the Au electrode (typically 100 nm thick).
The sample is secured to the sample holder with tungsten clips, and a shadow mask is screwed to the sample holder, so that the metal is finally evaporated only on certain areas of the sample (for samples not processed with EBL). A sketch of the setup for thermal evaporation is illustrated in figure 2.6.

An example of the fabricated devices is given in figure 2.7. On the right hand side a two contacts device is shown, that was fabricated via spin coating of GO on the entire substrate, with two gold pads evaporated with a shadow mask. On the left hand side, instead, a four-contact device is shown, obtained through electron beam lithography of the GO square on the middle of the substrate, on which the four gold pads are evaporated at the edges for the electrical contact, through metal evaporation with a shadow masks.

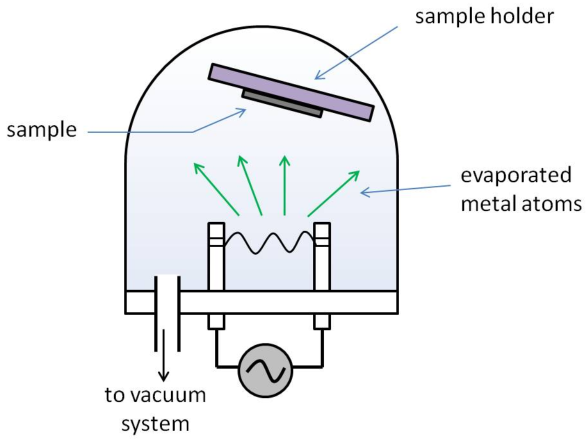

Figure 2.6: Sketch of the setup for thermal evaporation of metals.

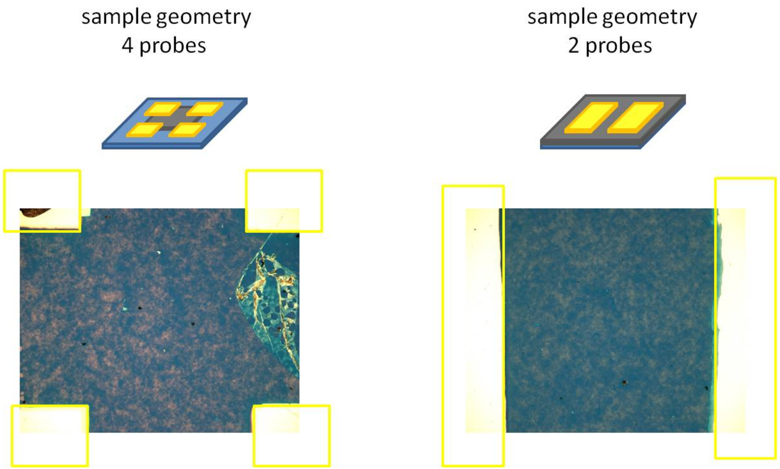

Figure 2.7: Left: four-probes sample geometry. Right: two-probes sample geometry.

2.5 Structural characterization

2.5.1 AFM imaging

Atomic force microscopy (AFM) [51] belongs to the family of the scanning probe microscopies (SPM), which are designed to measure local properties, such as height, friction, magnetism, conductivity and so on, on a small area of the sample. AFM is a powerful analytical tool for characterization of surfaces in the micro- to nanometer range. SPMs use a physical probe to scan the surface of the sample, and they produce an image dependent on which interaction is probed. In particular, AFM has been developed to measure the atomic force established between the tip and the surface of the specimen. The great advantage of the AFM over other SPM techniques is that it allows the investigation of any substrate, either metallic or insulating.

Normally, the probe is a sharp tip mounted on a cantilever. By using an optical setup, AFM measures the vertical and the lateral deflection of the cantilever induced by the tip-sample interaction. The optical setup consists in a laser which is reflected off the cantilever at the tip position. The reflected laser beam is then directed to a position-sensitive photo-detector consisting of four-segment photo-detector which retraces the angular deflection of the cantilever and thus the intensity of the analyzed force (figure 3.1).

AFM can operate in three different modes, depending on the selected distance between the tip and the sample, namely contact, non-contact and tapping mode (figure 2.9 A).

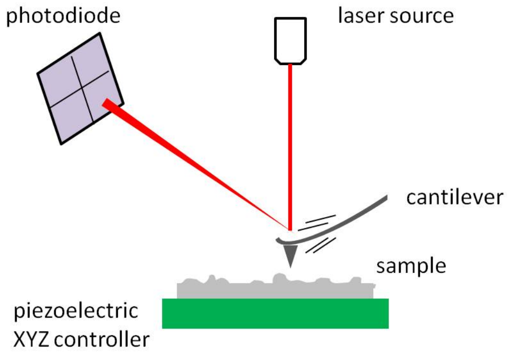

Figure 2.8: Sketch of the atomic force microscopy setup.

In contact mode, the AFM works in the repulsive forces regime. It uses a feedback to regulate the force on the sample. In this case, AFM not only measures the force on the sample but also regulates it, allowing acquisition of images at very low forces. The feedback loop consists of the tube scanner that controls the height of the tip, the cantilever and optical lever, which measures the local height of the sample and a feedback circuit that attempts to keep the cantilever deflection constant by adjusting the voltage applied to the scanner. A well-constructed feedback loop is essential for the microscope performances.

In the non-contact mode the AFM works at a distance in which Van der Waals attractive forces are dominant. The cantilever oscillates close to its resonant frequency; the interaction with the sample lower this frequency activating the feedback loop control which, adjusting the distance between the tip and sample, maintains a constant frequency or oscillation amplitude. The distance is recorded for all the scanned sample surface, giving a topographic image.

Finally, the tapping mode is used for delicate samples, because in this operation mode the duration of the interaction between the surface and the

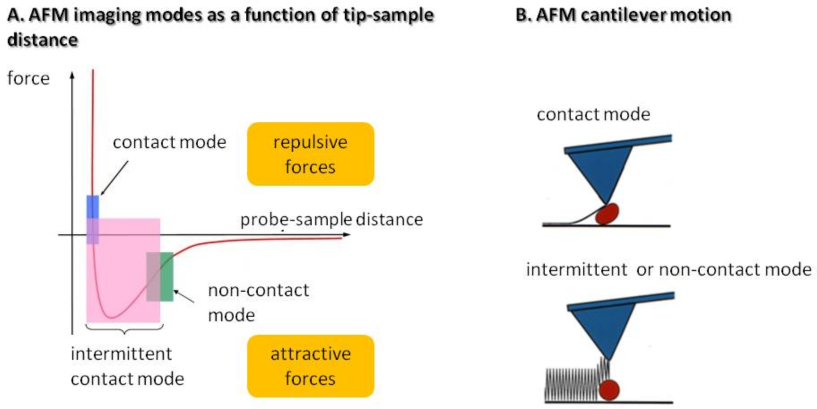

Figure 2.9: A) Lennard-Jones potential showing the tip-sample force as a function of their distance and B) a sketch of the motion of the cantilever for the different operating modes.

tip is negligible. In the tapping mode, again, the cantilever is allowed to oscillate close to its resonance frequency with wide oscillations, going from a non-contact to a contact region. The feedback control adjust the tip-sample distance in order to mantain the amplitude of the oscillations constant.

During this thesis work, an AFM Autoprobe CP (Veeco) at the A.F.M. Laboratory of the CIGS (Centro Interdipartimentale Grandi Strumenti of the University of Modena and Reggio Emilia) operating in non-contact mode has been used and the data were collected through PROSCAN DATA ACQUISITION software.

AFM imaging has been exploited for the morphological characterization of the GO films and to define the recipe of the deposition by spin coating in terms of the final film thickness. In this case, few squares of 100x100 μm^2 were obtained by EBL on several samples. The GO solution has been deposited by spin coating using different recipes. Thanks to the optimization of the spin coating parameters, the final result gives an homogeneous film of $\sim$5 nm each deposition (figure 2.10).

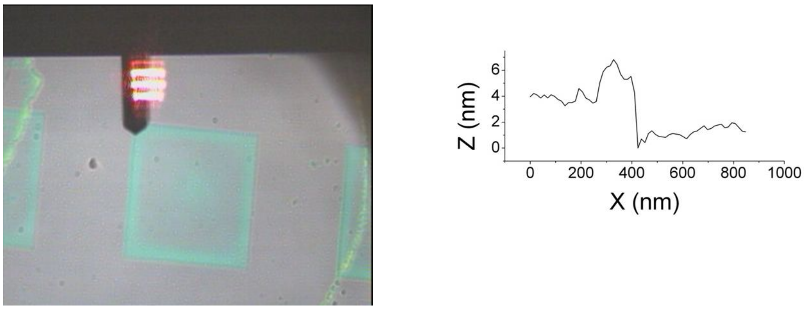

Figure 2.10: Optical image of squares of GO on Si/SiO$_2$ substrate obtained by EBL with the tip of the AFM measuring the step height (left) and the resulting height profile (right).

2.5.2 Micro-Raman spectroscopy

As discussed in section 1.4, Raman spectroscopy is a widely used technique to characterize graphitic materials, since it is non-destructive, fast, and can give many informations about the structure and the electronic and vibrational state of the analyzed sample.

Raman spectroscopy is based on the inelastic light scattering, or "Raman effect", which was firstly observed in 1928 by C. V. Raman and K. S. Krishnan in molecular liquids [52, 53].

When a sample is irradiated with an intense monochromatic light, usually coming from a laser, most of the radiation is scattered back at the same wavelength of the incoming light (Rayleigh scattering) while a small fraction of the scattered photons have a wavelength which is shifted with respect to the original one (inelastic light scattering). If the outcoming photon has a lower energy than the incident one, the process is called Stokes Raman scatter, while in the case it has a final energy which is higher than the incident light after the interaction with the sample, the process is called Anti-Stokes Raman scatter (figure 3.3). These two frequencies compose the Raman signal. The incident light will interact with the molecule, and depending on the vibrational state of the latter, Stokes or Anti-Stokes scatter will occur. In fact, the Stokes and Anti-Stokes Raman frequencies in molecular systems are associated principally with rotational, vibrational and electronic level transitions. Since the amount of energy change, either lost or gained, is characteristic of

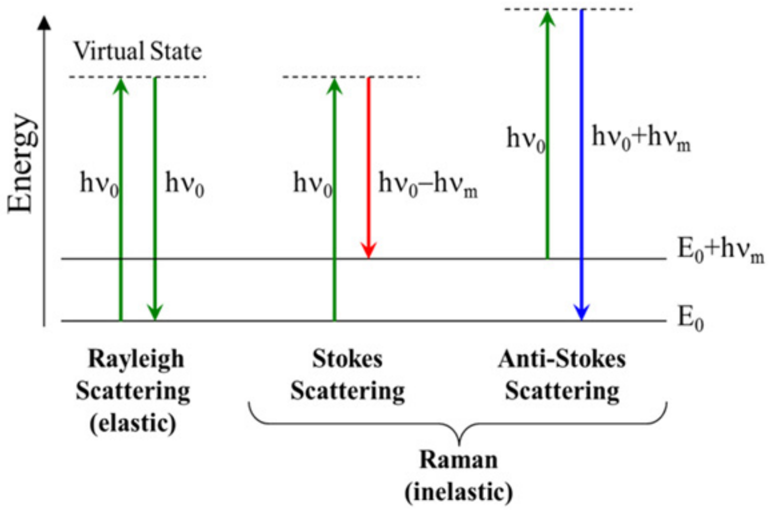

Figure 2.11: Jablonski diagram representing quantum energy transitions for Rayleigh and Raman scattering

the nature of each bond (vibration) present, it is possible to collect sufficient information for a very precise characterization of the molecular structure.

Along the identification of electronic and vibrational and rotational states in atoms and molecules, the Raman energy shift can be associated also to excitonic states in semiconductors, or phonon states in crystals, etc., making Raman Spectroscopy a very versatile and powerful technique.

The acquired spectrum shows the intensity of the scattered light as a function of the frequency difference with the one of the incident photons.

A typical setup for micro-Raman spectroscopy is illustrated in figure 2.12. It consists of a usual optical microscope equipped with a series of lenses, mirrors and filters to guide and manipulate the laser radiation coming from the source in order to carry the Raman signal to the spectrometer, which is usually a CCD camera.

Since the number of inelastically scattered photons is very small and the spot of the laser is such that only an area of about few μm^2 is analyzed, a radiation of high density is preferably used ($\sim 10^6$ W/cm^2), with the drawback of possible damages on the sample. To avoid this risk, the optical part of the setup is provided with optical filters to tune the radiation intensity.

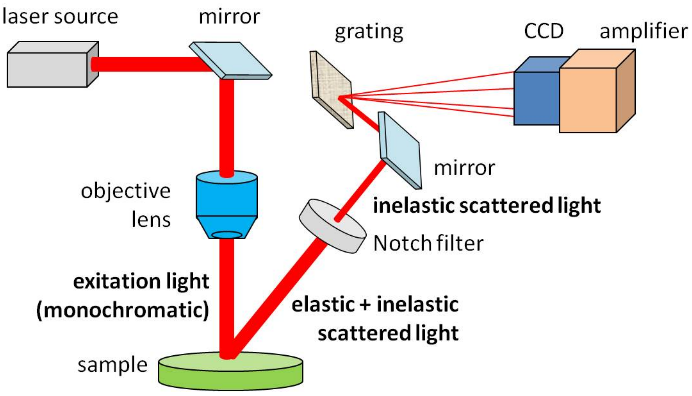

Figure 2.12: Illustration of typical micro-Raman spectroscopy setup.

The micro-Raman spectroscopy setup used during this thesis work is the LabRam Horiba Jobin Yvon (figure 2.13) at the Optical Spectroscopy Laboratory of the CIGS (University of Modena and Reggio Emilia). The laser source is He-Ne type (632.81 nm) with a maximum power of 20 mW, connected with an Olympus BX 40 Microscope (objectives 10x, 50x and 100x) and a CCD detector 1024 x 256 x 16 cooled by a Peltier cooler. Data were acquired by Labspec software and the spectra were then normalized in post processing.

A typical Raman spectrum of our GO thin films on Si/SiO$_2$ is presented in figure 2.14. It shows the two main features characteristic of the Raman spectrum of graphene oxide: the broad D peak at $\sim$1350 cm^{-1} and the G peak at $\sim$1580 cm^{-1} (see section 1.4 for more details).

Figure 2.13: LabRam Horiba Jobin Yvon at the CIGS labs in Modena.

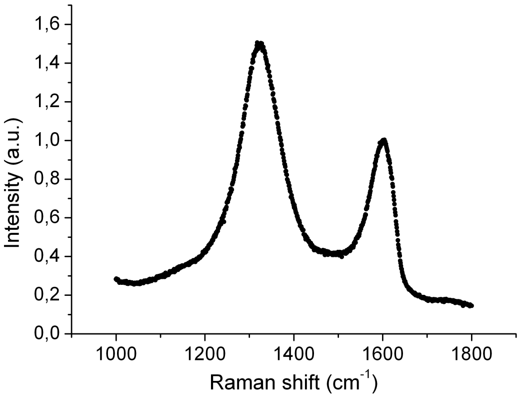

Figure 2.14: Typical micro-Raman spectrum of GO film 10 nm thick deposited by spin coating on Si/SiO$_2$.

2.6 Low temperature electrical characterization

The electrical characterization of the samples as a function of temperature has been carried out with a Quantum Design Physical Property Measurement System (PPMS) cryostat connected with an external Keithley 2636 Source-Meter, interfaced with a PC through a Labview software which I specifically realized and developed.
The cryostat allows to control the temperature from 1.9 K to 400 K, and is equipped with a superconducting magnet generating fields up to 7 T for the magnetic characterization.
The Keithley source-meter can work both in two probes and four probes configurations and is particularly suitable for low noise measurements of high-impedence devices, achieving current sensitivity in the sub-pA range, while being capable to generate DC voltage sources as high as 200 V.

The cryostat

The PPMS is composed by the following hardware components:

- nitrogen-jacketed dewar for the liquid helium bath
- probe
- top plate assembly
- vacuum pumping system
- electronics cabinet

The dewar contains the liquid helium bath in which the probe is immersed. The nitrogen-jacketed dewars is particularly efficient thanks to the layer of liquid nitrogen sandwiched between the superinsulation and the liquid helium, which further insulates the helium bath, as does the vacuum in the region between the liquid helium and the liquid nitrogen (see figure 2.15). The probe is immersed in the liquid-helium bath inside the dewar. The probe incorporates the basic temperature-control hardware, the superconducting magnet, the helium-level meter, the gas lines, the sample puck connectors, and various electrical connections. It is composed of several concentric stainless steel tubes. Its outer layer isolates the sample chamber from the liquid-helium bath. Two concentric tubes, separated by a sealed, evacuated region, prevent heat exchange between the sample chamber and the helium bath.

The bottom of the sample chamber is made of copper, in order to provide a region of uniform temperature. The very base of the sample chamber contains the connectors that contacts the installed sample puck. Then, two thermometers and a heater are immediately below the sample puck connector: the proximity to the copper sample puck helps to assure a good thermal contact during the experiments. The wiring for the sample puck runs up to the probe head.

The region between the sample chamber and the inner vacuum tube is referred to as the cooling annulus. Helium is pulled through the impedance tube into the cooling annulus so that it can warm and cool the sample chamber uniformly.

Electrical measurements

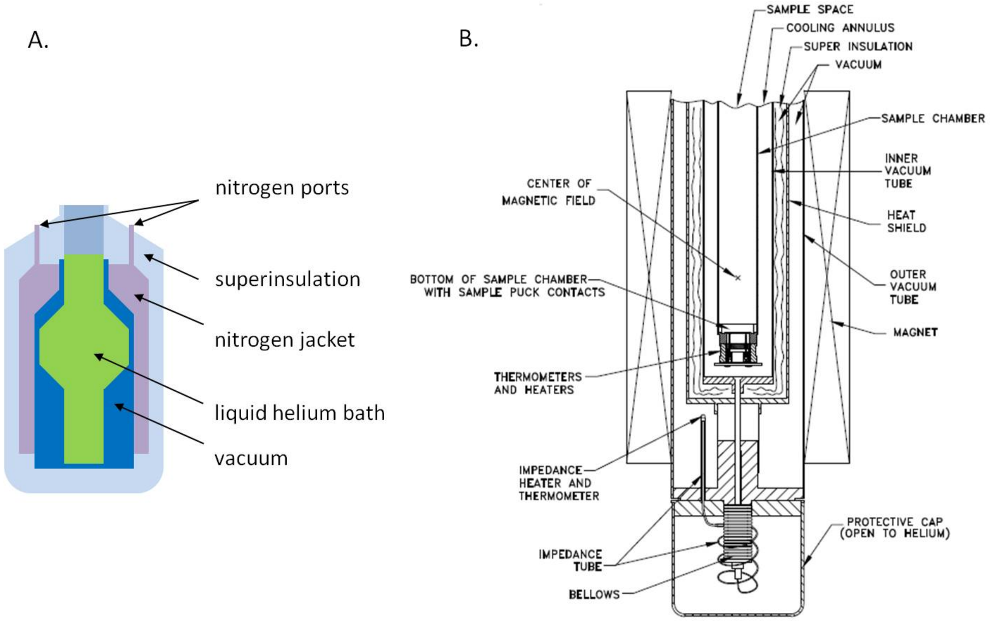

Figure 2.15: A. PPMS nitrogen-jacketed dewar for the liquid helium bath and B. PPMS probe major components. [54]

The electrical contacts between the metal pads on the sample and the cryostat sample puck are made thanks to an ultrasonic wire bonding machine (Kulicke and Soffa Model 4123 Wedge Bonder [55]), which allows one to solder gold wires between them.

In our samples, both the resistivity of the GO or rGO films and the so called contact resistance can be very high.

If the resistance were measured by a simple ohmmeter, the resistance of the cables and any resistance at the contacts would be measured as well as the resistance of the sample under test.

An usual technique to eliminate the contact resistance, in order to make sure that it does not affect resistance measurement, is to acquire measurements in the 4-point probes configuration with the van der Pauw method [56].

In the 4-point probes sensing, also called remote sensing, two of the probes are used to source current while the other two are used to sense the voltage. The separation of the current and the voltage electrodes allows one to elim-

inate the leads and the contacts resistances from the measurements.
The conventional configuration for 4-point probes resistivity measurements has the four electrical leads attached along a straight line, but often the accuracy of this method is limited by the difficulty to precisely determine the geometry of the sample.
To overcome this problem, it is more convenient to use the technique of van der Pauw to determine the resistivity of the sample.
The van der Pauw method uses four contacts placed at the edges of a flat homogeneous sample, and it is particularly useful because geometrical asymmetries among the contacts become unimportant.
Usually the electrical leads are placed at the four corners of a roughly square sample, as shown in figure 2.16 b.

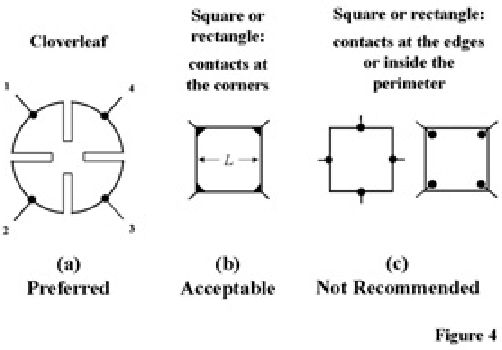

Figure 2.16: Possible contacts placements for van der Pauw method.

The resistivity is then calculated mathematically from the combination of eight measurements around the sample, as shown in figure 2.17:

$$\rho_{avg} = \frac{\rho_A + \rho_B}{2} \tag{2.2}$$

where

$$\rho_A = \frac{\pi}{ln2} f_A t_s \frac{V_2 + V_4 - V_1 - V_3}{4I} \tag{2.3}$$

$$\rho_B = \frac{\pi}{ln2} f_B t_s \frac{V_6 + V_8 - V_5 - V_7}{4I} \tag{2.4}$$

with t_s being the sample thickness, I the current run through the sample and V_{1-8} the measured voltages. The functions f_A and f_B are geometrical factors based on sample symmetry, and can be determined by voltage ratios, as explained in ref. [57]. For perfect symmetry, one has that $f_A = f_B = 1$.

Electrical characterization has been carried out both in two contacts configuration and in four-points probes configuration with the van der Pauw technique. By comparing the two methods, we could observe no substantial difference in the behavior of the resistance as a function of temperature and applied magnetic field, thus making the two contacts measurements preferable in terms of ease of the technique. Thus in the following chapters, when not differently specified, all the measurements are carried out in the two probes configuration.

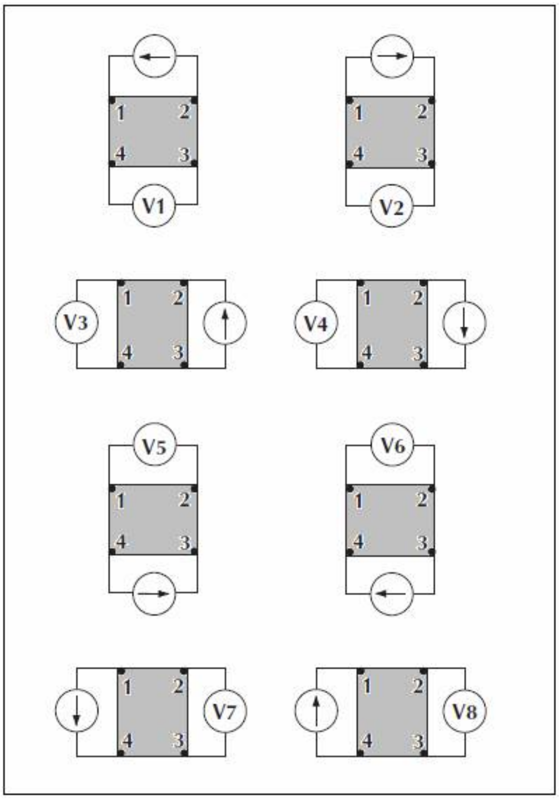

Figure 2.17: Van der Pauw resistivity measurement conventions.[57]

Moreover, for each measurements we carefully controlled and monitored that the I-V characteristic is linear in the used voltage range, in order to ensure that the contacts remain ohmic with changing temperature and/or magnetic field.

For the measurements of the resistance as a function of temperature, a reading voltage of 200 mV is typically used if not differently specified.

For the magneto-resistance measurements, a reading voltage of 100 mV or 200 mV is used, depending on the experimental conditions. The typical sweeping rate of the magnetic field used is 200 Oe/s, even though the same measurements have been performed at 50 Oe/s and 100 Oe/s to check the speed dependence, without finding any difference.

In figure 2.18 is shown the block diagram of the electrical connections used for the two-points probes measurements.

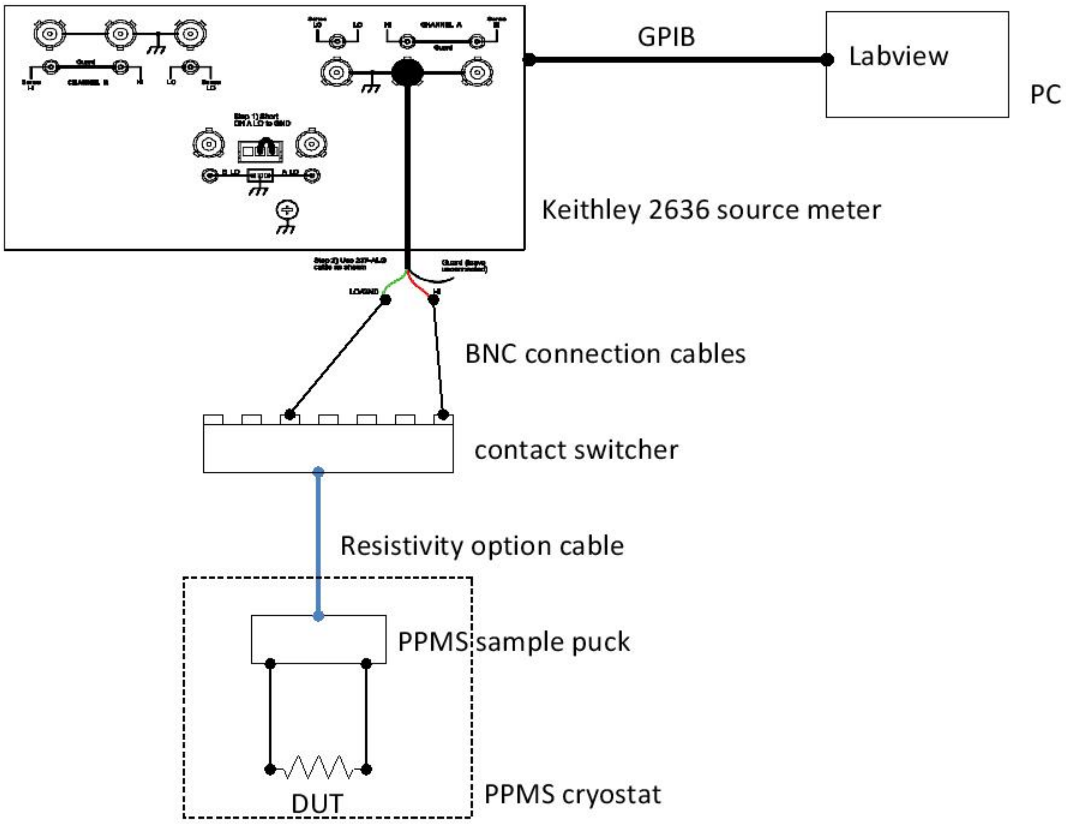

Figure 2.18: Block diagram of the electrical connections for the two-points probes configuration measurements.

Chapter 3

Thermal treatments: film characterization and *in-situ* resistance measurements

The following chapter contains the first part of the study about reduced graphene oxide: it concerns the analysis of the effects of the reduction by thermal annealing of the GO thin films. Indeed, great changes in the structure and in the electronic properties of GO films are expected as the reduction process occurs.
The investigation is carried out by scanning probe and spectroscopic techniques (AFM microscopy and micro-Raman analysis) and by the control of the resistance behavior during the reduction, by *in-situ* resistance measurements. It is well-known, in fact, that one of the major changes in graphene oxide due to its reduction is that it undergoes a transition from insulator to semiconductor or even semimetal, and a control of this process may give informations about the reduction mechanisms and efficiency.

3.1 Morphological characterization of the GO films

The deposited GO films have been characterized morphologically by AFM microscopy, in order to estimate the thickness of the film and its average roughness, and to highlight different substructures.

In this first part of the study, only solutions of GO with average flake size of 1-2 μm have been used.

To study the thickness, a hole of rectangular shape of 1x2 mm has been patterned with the EBL technique on a PMMA film on top of a Si/SiO$_2$ substrate. Then, the GO solution has been spincoated with the procedure exposed in section 2.2, and after the lift-off process, the thickness of the resulting film has been measured with AFM.

The section profile measured perpendicular to the GO edge reveals a film thickness of about 10 nm, as shown in figure 3.1.

Image 3.2 shows, instead, a typical AFM topographic map of the film with the relative height histogram.

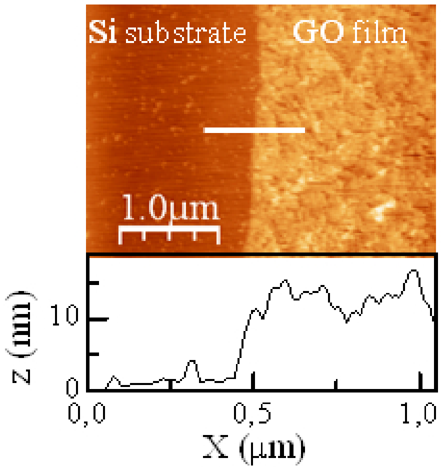

Figure 3.1: AFM image of 10 nm thick GO film deposited on Si/SiO2 substrate and below AFM section profile along the white line revealing the film thickness.

AFM roughness analysis was carried out employing the WSxM 5.0 software,

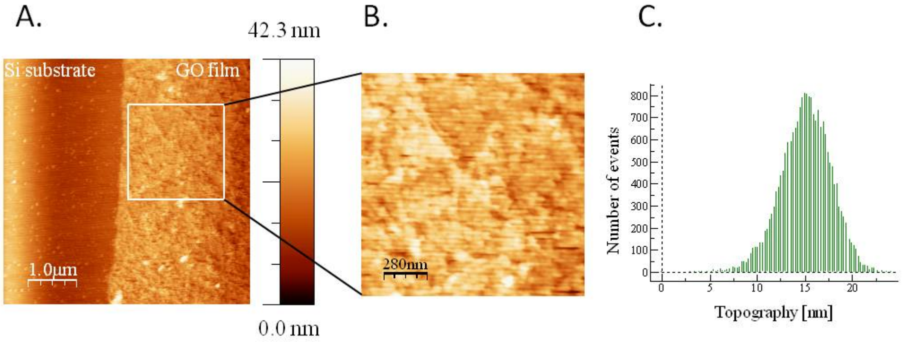

Figure 3.2: A) AFM image showing on the left the Si substrate and on the right the GO film, B) a magnification of the indicated area of the GO film and C) the height histogram.

and the resulting surface root mean square (RMS) roughness value of the GO film is 2.7 nm.

3.2 Micro-Raman spectroscopy

In order to characterize the reduction process of the GO films also from the structural point of view, we acquired Raman spectra for each sample before and after the thermal annealing, in order to estimate the changes in the structure of the film due to the reduction.

Figure 3.3 shows the acquired micro-Raman spectra for a typical as-deposited GO film and for rGO films annealed at different temperatures. The spectra show the two typical peaks of GO, respectively assigned to the D and the G bands (see section 1.4 for more details).

Structural information are generally then extracted from the spectra thanks to the empirical Tuinstra-Koenig relation (1.1), which relates the intensities of the D and the G peaks, respectively I_D and I_G, to the size of the sp^2 clusters (see equation 1.1).

Figure 3.4 shows the measured I_D/I_G ratio for the set of samples annealed in high vacuum at different temperatures. Each point corresponds to a different sample, as for each sample the reduction process was carried out only once at a single temperature. The fit of the two peak has been done with two

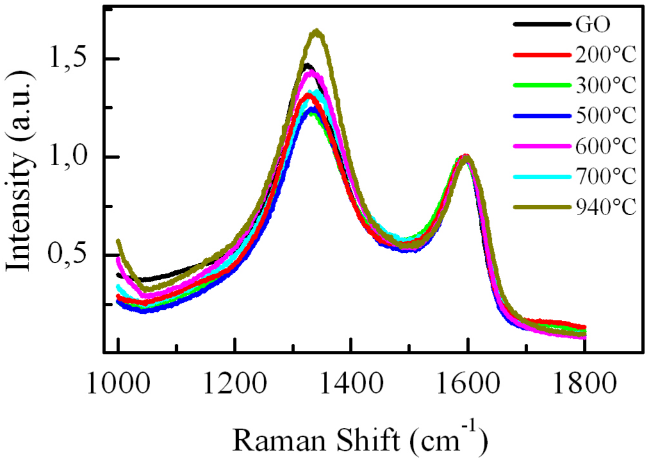

Figure 3.3: Raman spectra of as-deposited GO film and of samples reduced in high vacuum at different temperatures.

Lorentzian shapes using OriginPro 8.5 software.

The top panel shows the ratio found for the as-deposited GO, while in the bottom panel the intensity ratio is calculated from the Raman-spectrum acquired after the thermal annealing.

The intensity of the D peak increases over the G peak as the reduction progresses with increasing annealing temperature, in agreement with previous reports [30, 38, 36, 58, 21]. The increase of the I_D/I_G ratio can be explained, keeping in mind the Tuinstra-Koenig relation 1.1, as the creation of a high number of new graphitic domains smaller in size than those present in the GO before the reduction.

We point out, however, that I_D/I_G ratio measured before reduction presents a very high dispersion, which – we believe – makes the Raman analysis not sufficiently accurate to reliably reveal the morphology of the rGO film and to give indications about the reduction efficiency. Nevertheless, I_D/I_G ratio values after the reduction are in agreement with previous literature ([27] and references therein).

We also investigated in detail the presence of the 2D peak at ∼2690 cm^{-1}, which corresponds to the second order of the D-band, but no recognizable peak has been measured for our samples.

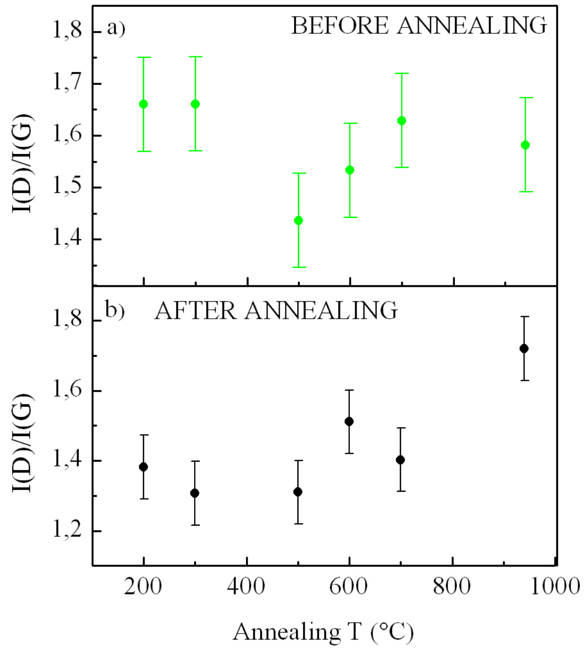

Figure 3.4: Ratio between D peak and G peak intensities of the Raman spectra a) before the reduction for the different samples and b) after the reduction as a function of the annealing temperature. The high dispersion of the I_D/I_G ratio values reported for as-deposited GO makes our Raman data not sufficiently reliable for an accurate morphological characterization of the reduction efficiency.

3.3 *In-situ* resistance measurements

We monitored the reducing effect of the thermal annealing by measuring the *in-situ* resistance of the films as a function of time, during the process in argon flow.

sample	a (mm)	b (mm)	T_a°C	δt
A	2.3	6.5	300	21h15min
B	0.8	5.0	300	21h15min
C	1.7	5.0	300	50min
D	1.7	4.5	400	18h
E	1.3	5.0	400	2h
F	1.2	4.3	400	4h
G	1.8	3.4	500	4h
H	1.4	4.7	500	2h
I	1.3	3.8	500	8h

Table 3.1: Measured samples with relative channel size a and b, annealing temperature T_a and duration of the treatment t.

The samples are films of GO with thickness of 10 nm, over which gold electrodes are thermally evaporated. The dimensions of the channel lengths of the measured samples are reported in table 3.1.

The thermal annealing is carried out in argon atmosphere controlled by a flow-meter, at temperatures of 300°C, 400°C, 500°C and 600°C. The duration of the treatments is varied between 50 min and 21 h to study the time dependence.

The measurements are carried out with the setup shown in figure 2.1 with a Keithley 2636 Source-Meter, applying a reading voltage of 200 mV.

Fig 3.5 shows a typical *in-situ* resistance measurements as a function of time. The sample holder is provided with a thermocouple at the sample position, so that it is possible to monitor the sample temperature. The green dots in figure 3.5 represents the temperature profile of the sample.

Initially the sample is out of the tube furnace at room temperature. The resistance of the film is very high (above 1 GΩ) as expected, because as-deposited GO is an electrical insulator. At a certain time, indicated with the red arrow, the sample is moved into the pre-heated tube furnace. The measure is quite noisy at this point because of the movement of the sample holder and the electrical connections. After a short time interval where the sample starts to heat up, the measurement shows a very fast resistance drop.

In this short time, typically less than 5 minutes, the reduction occurs: the residual water evaporates and the functional groups are released. After few

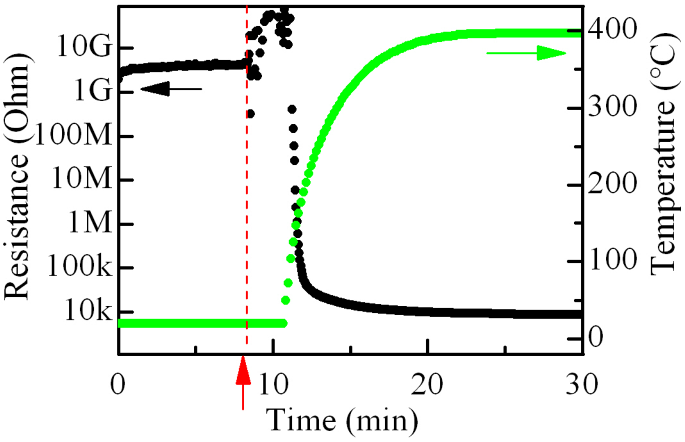

Figure 3.5: Black dots: typical *in-situ* measurements of the resistance of a GO sample before and during the thermal annealing in the tube furnace in argon flow. Green dots: relative temperature profile of the treated sample. Red arrow: time t at which the sample is pushed into the preheated tube furnace for the annealing.

minutes the resistance reaches a saturation. In this second part of the process, probably structural rearrangements still occur, but the relative change in the resistance is smaller than the sensitivity of our measurement setup.

Indeed, one may think that the structural rearrangement could be just a slower process than the fast oxygen release. To investigate this in more details, we measured the resistance as a function of time of different samples annealed at the same temperature, changing the duration of the treatment (see table 3.1).

Figure 3.6 shows the resistance measurement for sample D and sample E, which are respectively annealed at 400°C for 18 hours and for 2 hours. After the initial drop, when the sample is introduced into the tube furnace, the resistance settles at a certain value for both the samples, and it does not change until the sample is allowed to cool down. Even for sample D, during the 18 hours into the tube furnace, we do not report further development of the resistance, and the final values for both the sample are comparable within the error bar.

This shows that although the whole reduction process is governed by two main contributions, i.e. a oxygen loss and a consequent structural rearrangement, they are both fast and occur in the first few minutes of the thermal treatments. Still, it may be that the structural modifications keeps occurring for longer time, but our experimental setup is not sensitive enough to reveal it, and thus we can not extract any information about this process.

To further analyze the effects of the thermal annealing, we measured the current as a function of the applied voltage before and after the treatment (once the sample is cooled back to room temperature).

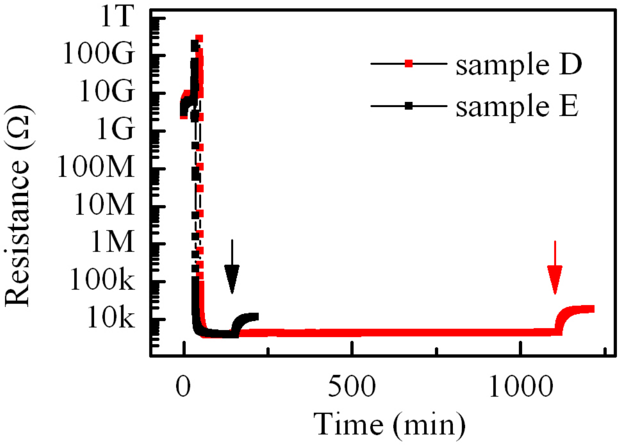

Figure 3.6: Resistance as a function of time for sample D and sample E (see table 3.1), both annealed at 400°C with different annealing time. Arrows indicate where the sample is pulled out the tube furnace and allowed to cool down in argon flow.

Before the treatment, the measured current is below the instrumentation limits, showing that GO is highly resistive (insulator). After the thermal annealing, instead, for all the annealing temperatures, we found linear I-V characteristics, indicating that the graphene oxide films acquired a certain electrical conductivity and ohmic conduction is established (figure 3.7).

These results strongly suggest that the GO films after the thermal annealing are already reduced (even if at different degrees) for all the different temperatures used in the study.

Figure 3.8 reports the values of the sheet resistance of the rGO films as a function of the annealing temperature, measured once the samples are cooled

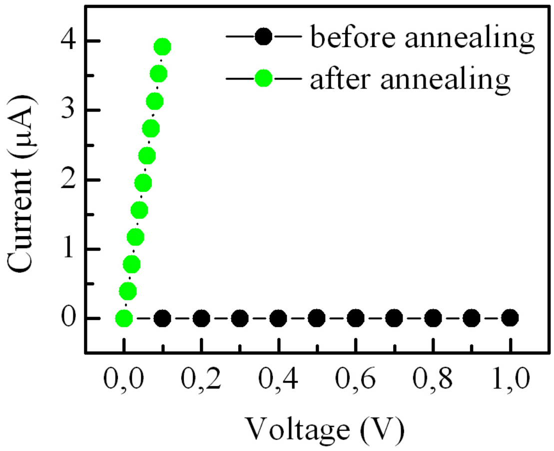

Figure 3.7: The measured I-V characteristic curve for sample D before (black dots) and after (green dots) the thermal treatment at 400°C.

at room temperature. As shown, the final sheet resistance becomes smaller with increasing annealing temperature. The value dispersion for the samples treated at 300°C is due to the mild annealing which leads to final results which can vary considerably.

For annealing temperatures ≥600°C, instead, we observed a loss of material

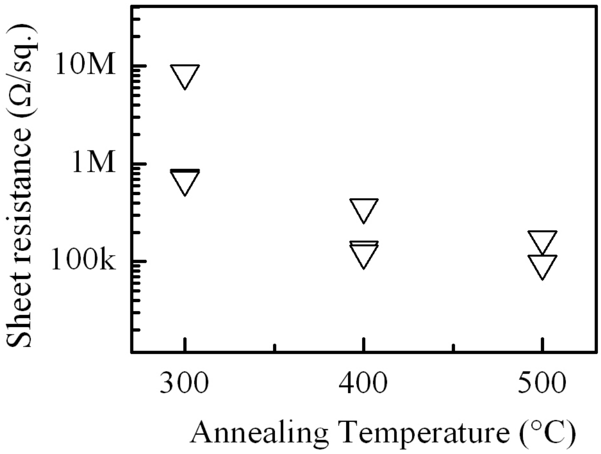

Figure 3.8: Final sheet resistance of the rGO films as a function of the annealing temperature.

of the sample, in some cases even leaving the surface of the substrate almost clean. This is likely due to the residual oxygen which is still present in the argon atmosphere. The oxygen may react with the surface of the GO film, eventually leading to a complete loss of the sample.

This is the reason why, in the next chapters, only the annealing in high vacuum ($\sim 10^{-6}$ mbar) is performed as the standard protocol for the GO thermal reduction.

3.4 Reduction process characteristic time

To give a deeper insight into the thermal reduction process, we studied the characteristic time of the drop of the resistance.

To do this, we analyze only the time interval in which the resistance shows the sharp decrease, which begins at the moment in which the system has enough energy to start to release the functional groups, thus restoring the sp^2 network and recovering the electrical conductivity of graphene-like domains. The resistance drop ends when the major changes already occurred and there is only a fine rearrangements of the structure left (fig. 3.9 A).

In this interval, we can suppose an exponential dependence of the resistance on time, such as:

$$R \propto \exp \frac{-t}{\tau} \tag{3.1}$$

where τ is the characteristic time of the process.

Figure 3.9 B) shows the value of τ extrapolated from the fits, as a function of the annealing temperature. The process is faster for increasing annealing temperatures, and the characteristic time went from ∼8 s to ∼1 s, as the annealing temperature is increased from 300°C to 600°C.

Although the time scale is only approximate, due to the not perfect isothermal conditions in which the measurements are performed, the reduction process characteristic time scales correctly with the annealing temperature, as one may expect (see figure 3.9 B.). This process, in fact, is thermally activated, and thus it is faster for higher temperatures. Most of the changes due to the reduction happen just at the moment when the system reaches enough energy thanks to the temperature, while only small developments occur after that point.

This is consistent with results reported in literature, where thermal annealing lasting only few minutes are used (for example Mattevi *et al.* used thermal annealing duration of 15 min [27]), and there is no evidence for different efficiencies if longer times are used.

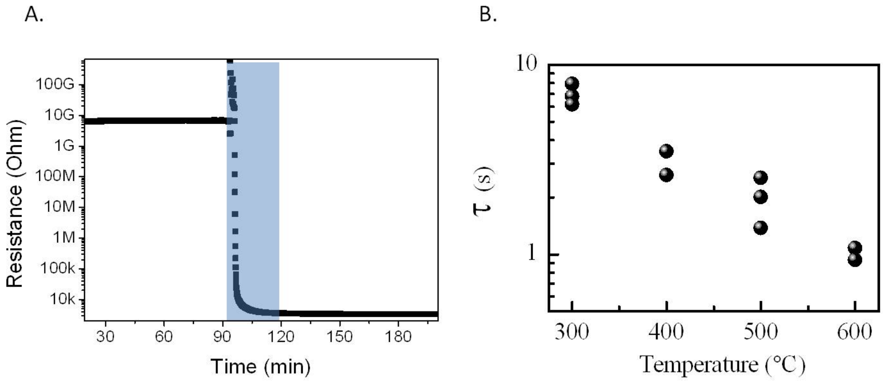

Figure 3.9: A. Resistance measurement as a function of time for thermal treatment at 400°C, with highlighted the range of the fit, and B. characteristic time of the process as a function of annealing temperature (each dot corresponds to a different sample treated at the same temperature).

3.5 Activation temperature of the reduction process

Based on the previous section, one may conclude that the process of reduction begins already before that the sample reaches the tube furnace temperature, at temperatures even lower than 300°C (the lowest temperature analyzed in the present work).

Indeed, this is confirmed by a measurement of the resistance as a function of time (figure 3.10), where the protocol adopted is the following: the sample is placed inside the tube furnace while the latter is still at room temperature. The tube furnace is then heated at 5°C/min while the current running through the sample is monitored (V reading is set equal to 0.2 V).

The measured current is zero at the beginning of the experiment. At a certain time, it shows a fast increase, and that time corresponds to a temperature of about 220°C (see the temperature profile of figure 3.10).

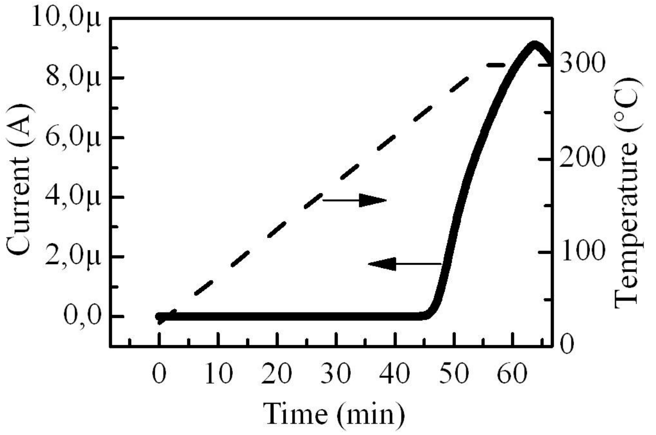

Figure 3.10: Current (solid line) and temperature profile (dashed line) vs time in a *in-situ* resistance measurement.

This shows that the activation temperature of the reduction process is just above 200°C: the GO film starts to release the excess water and the functional groups attached to the surfaces. This give rise to the creation of sp^2-hybridized domains and conductive pathways form in the structure.

In a second step, which depends on the actual temperature of the process, the system, while keeping loosing residual functional groups, also undergoes to local rearrangements of the structure. This second change determines the final features of the rGO, also in terms of structural order and electrical properties.

To better visualize the effect of these second part of the reduction process, temperatures greater than 500°C are needed. Thus, to avoid the material loss, thermal annealing was carried out in vacuum in all the following experiments.

3.6 Conclusions

In conclusion, we characterize the GO film by AFM imaging and we investigated the structural changes due to reduction by micro-Raman spectroscopy. We were then able to monitor directly the reduction process by *in-situ* resistance measurements, controlling the evolution of the GO film from being an insulator to an ohmic conductor.

Micro-Raman spectroscopy showed that, after the thermal reduction, the structure of the rGO film presents a high number of sp^2-hybridized domains. Through the Tuinstra-Koenig relation, it was possible to show that the number of graphitic domains increases with increasing annealing temperature, thus reporting a relative better quality of the rGO.

We then saw a direct connection between the annealing temperature and the final sheet resistance of the film, confirming that higher temperatures lead to a higher level of reduction of the graphene oxide and thus a lower sheet resistance.

To study in deeper details the reduction process by thermal annealing, we analyzed the characteristic time of the *in-situ* resistance measurements, finding that the main changes – which we ascribed to functional groups released from the surface and residual water evaporation – occur in the very first time interval. It was not possible to establish the correct timescale because of the non-isothermal conditions of the measurements, but we correctly reported that, as the process it thermally activated, it is faster for higher annealing temperature.

We finally showed that the activation temperature for the thermal reduction is $\sim$200°C.

During *in-situ* resistance measurements, we experienced that residual oxygen in the annealing camera is very critical for the thermal reduction results, and particular care must be taken when the annealing is performed in some inert gas atmosphere when not in vacuum.

In order to study the electrical transport for higher level of reduction of graphene oxide thin films, higher annealing temperatures are needed. To overcome the problem of the material loss, thermal annealing has to be done in vacuum, where *in-situ* resistance measurements are not possible for our setup architecture, thus excluding direct observation of the reduction process progress.

Chapter 4

Charge carrier transport

One of the most attractive properties of graphene oxide is that it can be reduced to graphene-like conjugated structure thanks to the possibility to remove the oxygen-containing groups attached to its surface. This leads to the formation of conductive pathways which allows electrical transport throughout the sample. Moreover, the electrical properties of rGO can be tuned by the degree of reduction, which in turn can be controlled by simple fabrication protocols. This peculiar property makes rGO very attractive for applications in many fields, and a better understanding of transport in rGO could widen the potential of this material.

In this chapter it is presented a systematic study of the electrical properties of thermally reduced GO films, which were prepared at several reduction levels in a controllable way, i.e. by changing the annealing temperature. It has been possible to achieve distinct resistive states of rGO, which allow us to control the rGO electrical characteristics through a simple fabrication protocol. We also studied the magnetic field dependence of the resistance, finding a non-saturating negative magnetoresistance exceeding 60% at 2 K. The last section of the chapter deals with the dependence of the electrical properties of rGO with the size of the flakes forming the thin film.

The characterization has been carried out by resistance measurements from room temperature down to 2 K and under magnetic fields up to 7 T.

4.1 Samples characteristics

The set of samples analyzed in this chapter is fabricated as described in chapter 2.

To control the flake size, we diluted the solution of GO in distilled water until we reached the deposition of isolated single flakes on Si/SiO$_2$ substrate. The resulting sample was then investigated with SEM analysis to record the size of each individual flake. Before that, the sample was annealed at 400°C in high vacuum for 1 h to enhance contrast for SEM imaging. We recorded the size of approximately 100 different flakes, and we show in figure 4.1 (right) the resulting distribution.

The average size of the flakes was 1-2μm.

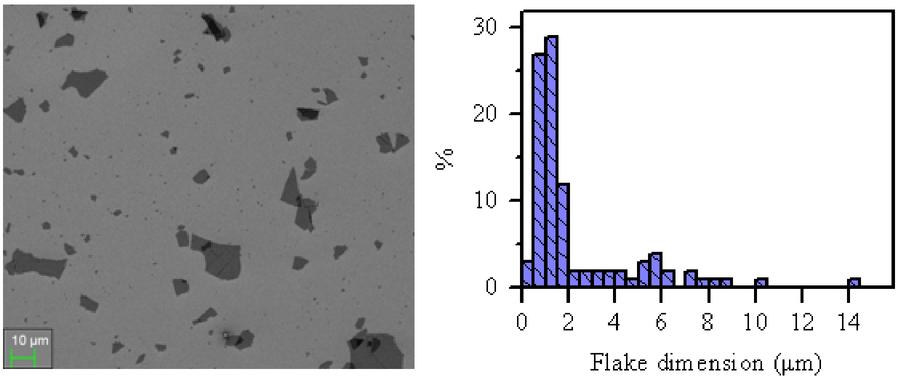

Figure 4.1: (left) Typical SEM image of the diluted GO solution after deposition on the substrate, and (right) flake size statistic.

The non-diluted GO/water solution has been spincoated on Si/SiO$_2$ substrate using the recipe described in section 2.2, so that we ended up with homogeneous films with thickness ~10 nm.

Then the samples have been thermally reduced in high vacuum (10^{-6} mbar) thanks to the setup shown in fig.2.2. Heat treatments were carried out at 200°C, 300°C, 500°C, 600°C, 700°C and 940°C for 1 h. We denote samples annealed at these temperatures as sample A, B, C, D, E and F, respectively. Geometrical details are given in table 4.1.

sample	Channel length (mm)
A	0.85
B	0.8
C	0.65
D	1.3
E	0.85
F	1.2

Table 4.1: Distance between the two gold electrodes for the different samples measured.

After the heat treatment, samples were kept in vacuum out of the furnace while they cooled down naturally.

4.2 Electrical transport at room temperature

Before the reduction, the resistance of the samples is above the instrumentation limits, confirming the insulating nature of the pristine GO. After the annealing, the IV characteristics become linear in the range of ±500 mV, indicating that ohmic conduction was activated for all the heat treatments we have done. Even for heat treatment at temperature as low as 200°C, the sample acquired a measurable electrical conductivity, confirming that reduction of GO is already activated at this temperature, as extensively discussed in the previous chapter.

From the linear IV curves we extracted the room temperature (RT) resistivity ρ_{RT}, which decreases by more than 2 orders of magnitude by increasing the annealing temperature (figure 4.2). ρ_{RT} for sample A is ~0.04 Ωm while for sample F is $\sim 1.02 \cdot 10^{-4}$ Ωm. The increase of the annealing temperature (T_A) results in a decrease of the room temperature resistivity of the samples, which reflects a higher level of reduction of our GO. ρ_{RT} drops very fast by increasing T_A up to 700°C, then it saturates for higher T_A. It is likely, that even though the graphene oxide is more reduced, and thus the sp^2 conjugated network is better restored, the transport is still limited by the increase of topological defects and structural disorder introduced by the high temper-

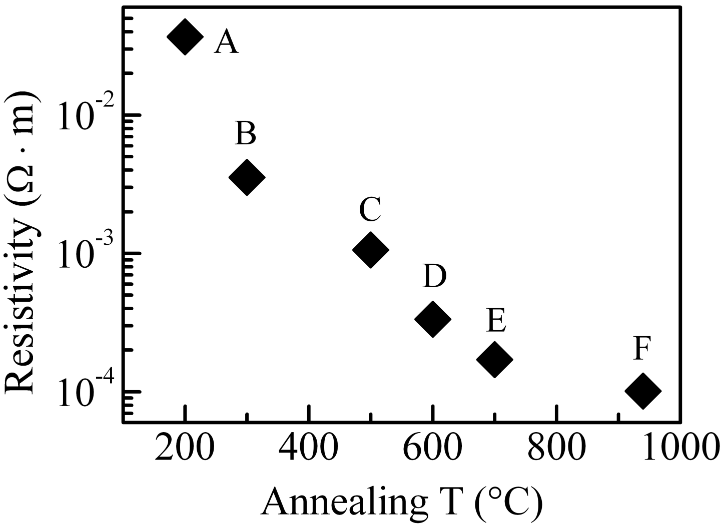

Figure 4.2: Room temperature resistivity of the rGO films as a function of the annealing temperature.

ature of the treatment. This prevents GO from fully recovering the electronic properties of pristine graphene [59, 43, 60]. Jung et al.[49] reported similar results of rGO resistance as a function of sp^2 carbon fraction.

4.3 Electrical transport at low temperature

In order to study the transport mechanisms in the rGO films, we measured the resistance (R) as a function of the temperature (T), from room temperature down to 2 K. The R(T) curve may increase up to 5 orders of magnitude upon cooling (figure 4.3).

Samples A, B, C and D become too resistive to be measured down to 2 K, so their R(T) curves span a smaller temperature range. We observe that the slope of resistivity increases faster by decreasing the degree of reduction of our GO.

For a generic thermally activated charge transport, R(T) can be expressed as:

$$R(T) = R_0 \exp\left(\frac{T_0}{T}\right)^p \tag{4.1}$$

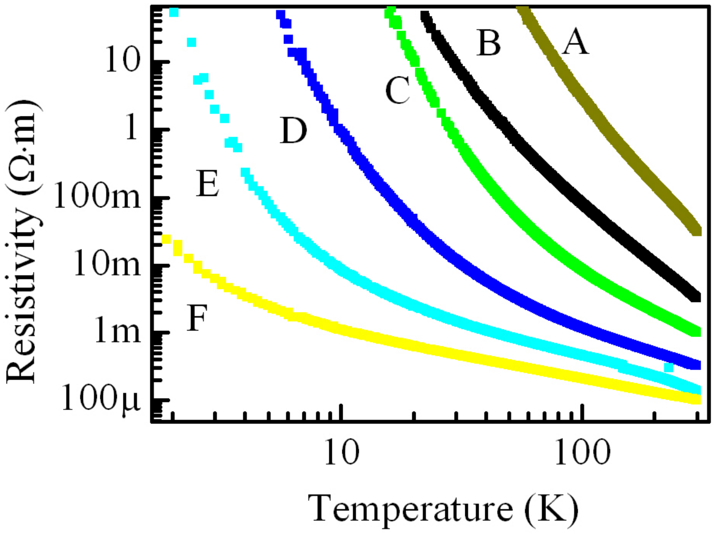

Figure 4.3: Resistivity as a function of temperature.

where T_0 is the characteristic temperature of the activation process. In the case of hopping-type charge transport, p is the exponent which discriminates between different mechanisms and it is equal to p = 1/(D + 1), with D being the dimensionality of the system [42]. In particular, the exponent p results to be equal to 1/3 for 2D Mott-VRH, 1/4 for 3D Mott-VRH, 1/2 for 2D Efros-Shklovskii VRH or 1 for nearest neighbor hopping transport mechanism with Arrhenius-like dependence.

The behavior of the resistivity was analyzed by plotting the natural logarithm of ρ as a function of the four different power laws accounting for different temperature dependencies. In figure 4.4 we show an example of the comparison between the different transport models for sample E.

As evident in figure 4.4 we cannot find a single regime that extends in the whole temperature range we have studied, but this is not surprising, since disordered materials quite often exhibit more than one ρ(T) law in such a broad temperature range. Yet we can recognize that specific ρ(T) dependencies appear systematically in all the reduced GO samples resistivity curves with a progressive extension of the interested temperature interval. In particular, taking into account all the different curves for all the samples, we

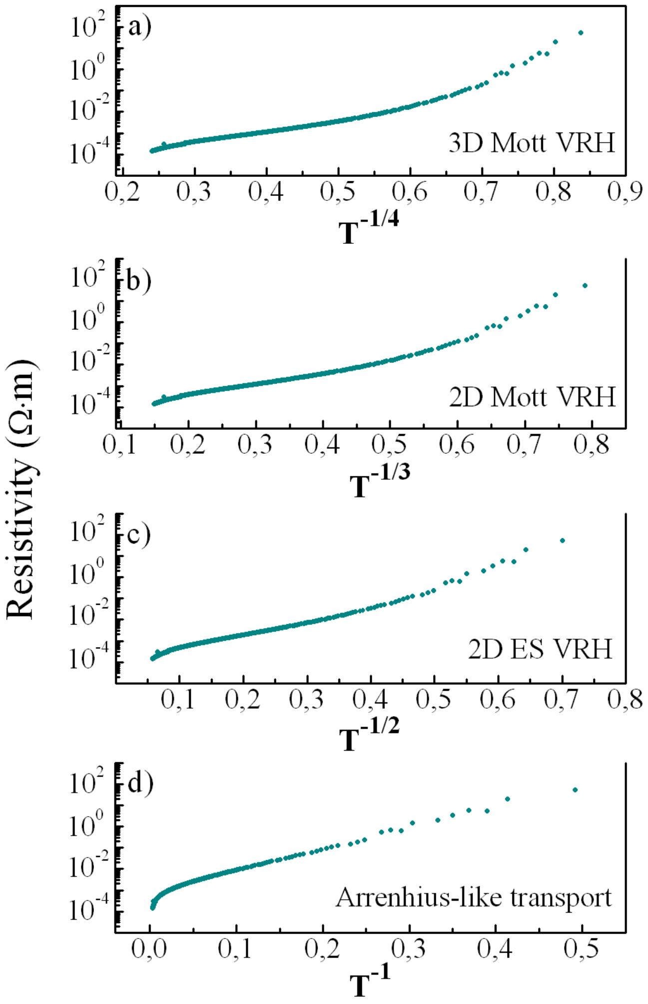

Figure 4.4: Comparison between the different transport model: log(ρ) for sample E as a function of T^{-x}, x being equal to (a) $x = 1/4$ corresponding to 3D Mott VRH, (b) $x = 1/3$ corresponding to 2D Mott VRH, (c) $x = 1/2$ corresponding to 2D ES-VRH, and (d) $x = 1$ corresponding to Arrhenius-like transport.

find that the $R = R_0 \cdot exp(T0/T)^{1/3}$ law spans the largest temperature range in all our samples: down to around 50 K, we actually find that experimental data of all our samples fit well the with 2D Mott VRH model.

To show that the $R = R_0 \cdot exp(T0/T)^{1/3}$ is probably the most representative law for our set of data, we plot the resistivity in a semi-log plot as a function of $T^{1/3}$ (figure 4.5).

Interestingly, the slopes of the linear fits scale with the degree of reduction of our GO.

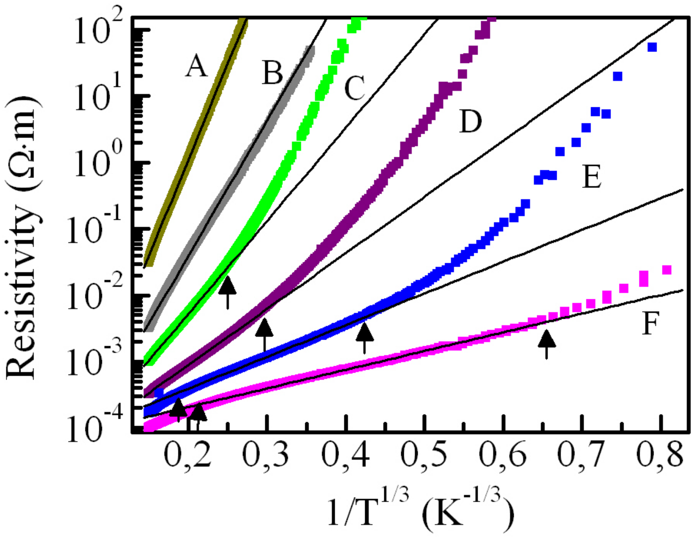

Figure 4.5: Resistivity vs $1/T^{1/3}$ for different values of annealing temperature. Black arrows indicate the temperature at which a crossover from 2D-Mott VHR (black lines) to another activated regime takes places.

Within the framework of the Mott-VRH model, the characteristic temperature T_0 of the $R = R_0 \cdot exp(T0/T)^{1/3}$ equation is given by:

$$T_0 = (3/k_B N(E_F)\xi^2) \tag{4.2}$$

where $N(E_F)$ is the density of states near the Fermi energy and ξ is the localization length.

The values of T_0 extracted from the fits scales down with increasing T_A (figure 4.6).

Considering characteristic values of $N(E_F)$ ranging between 10^{14} and 10^{16} cm^2 eV^{-1} with increasing grade of reduction of the GO, we obtain localization length ξ ranging between 1.2 nm and 4.1 nm, which are typical sizes of graphitic domains in rGO [59, 27, 49, 28].

The R_0 values derived from the 2D Mott VRH fits collapse to almost the same value, ranging from $3 \cdot 10^3 to 14 \cdot 10^3 \Omega$ (figure 4.7).

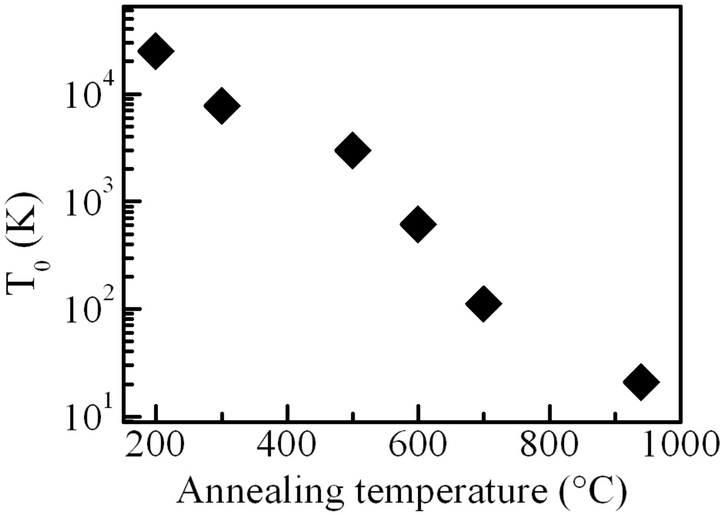

Figure 4.6: Characteristic temperature T_0 extracted from the $R = R_0 \cdot exp(T0/T)^{1/3}$ fit.

While for samples A and B (T_A = 200°C and 300°C, respectively) exper-

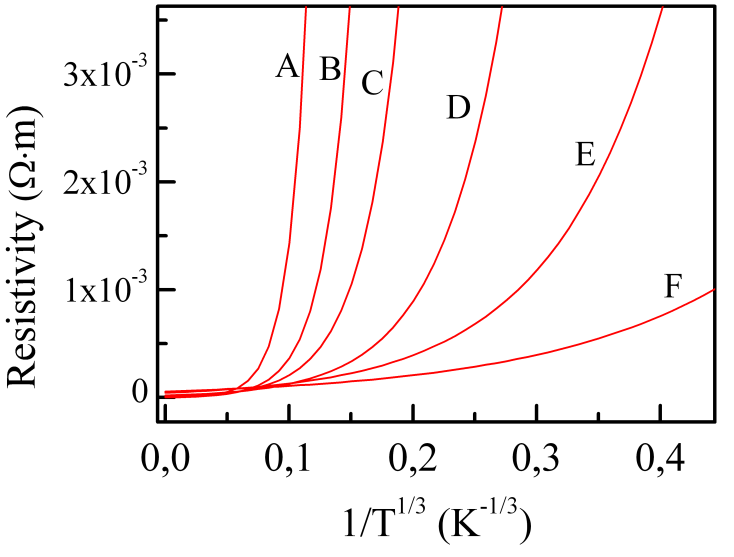

Figure 4.7: All the 2D Mott VRH fits collapse to almost the same R_0 parameter.

imental data fit the $R = R_0 \cdot exp(T0/T)^{1/3}$ law in the whole temperature range (down to 22 K for sample B), for more reduced GO, we observe deviations that occur at a crossover temperature T_c (marked by black arrows in figure 4.5) which scales with the degree of reduction, going from 64 K for sample C (T_A = 500°C) to 3.6 K for the sample F (T_A = 940°C).

The $R = R_0 \cdot exp(T0/T)^{1/3}$ behavior reflects the 2D dimensionality of the structure of the sheets. It has been proposed [27, 28, 61] that the reduction of GO produces islands of intact graphene separated by clusters of point defects within a graphene flake. Hopping presumably occurs between the intact graphene regions by consecutive inelastic tunneling processes. The scaling of the slope of the R(T) curves with increasing annealing temperature clearly indicates a gain in the electrical conductivity due to a decrease of defects density and the restoration of π-π bonds. Below the temperature T_c, a change of the electrical transport regime likely occurs.

For disordered systems it is in fact possible to see crossovers between different regimes by lowering the temperature, due to the fact that the system's characteristic lengths change. However, from our data it is not possible to pinpoint the actual transport regime below T_c: the investigated temperature range is indeed too small to allow a clear discrimination.

For samples E and F (T_A = 700°C and 940°C, respectively) we also observe a crossover (at T = 153 K and T = 103 K, respectively) to a different regime characterized by a R(T):

$$R = R_0 exp(E_g/k_B T) \tag{4.3}$$

where E_g is the activation energy and k_B is the Boltzmann constant (figure 4.8).

This is characteristic of an Arrhenius-like behavior [45] where 3D thermally activated processes start to dominate the conduction. Data fitting with $R = R_0 exp(E_g/k_B T)$ law gives activation energies of 26.5 meV and 11.7 meV for sample E and F, respectively, which are in good agreement with previously reported values [44, 45, 47].

The crossover from the 2D Mott-VRH to thermally activated regime is probably due to a increase of the characteristic lengths of the disordered 2D system

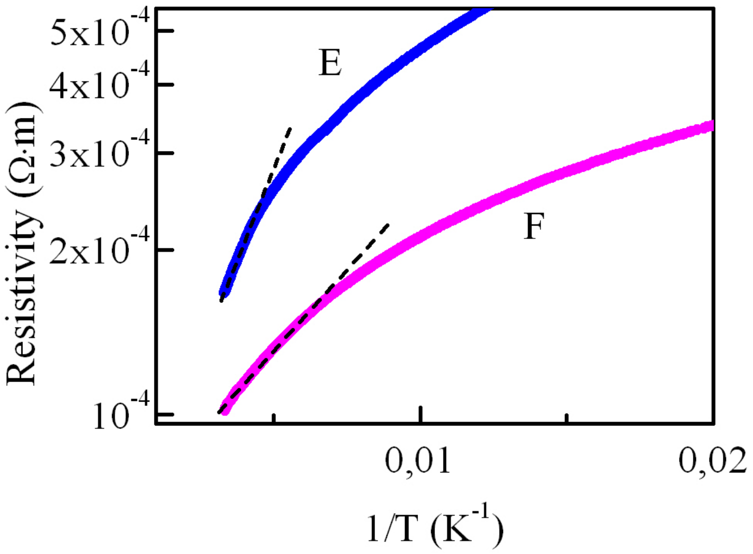

Figure 4.8: Arrhenius plot of resistivity for sample E and F.

and the beginning of a 3D conduction of charge carriers through the rGO film.

4.4 Magnetotransport

We have also studied the dependence of the resistance on an external magnetic field B applied perpendicular to the plane of the GO film. Samples A, B, and C turned out to be too resistive and the magnetoresistance $\Delta R/R = [R(B) - R(B=0)]/R(B=0)$, if any, is found to be within the electrical noise; therefore, we report the magnetoresistance data only for samples D, E and F (T$_A$ = 600°C, 700°C and 940°C, respectively).

For all of our samples we find a room temperature negative magnetoresistance (see figure 4.9).

However, while sample F shows negative magnetoresistance down to the lowest temperature, for sample D and sample E we observe a change to positive magnetoresistance (figure 4.10 and 4.11) at a temperature that is comparable to the one where the crossover in ρ(T) was observed (figure 4.12).

Negative magnetoresistance in rGO samples has been also reported in

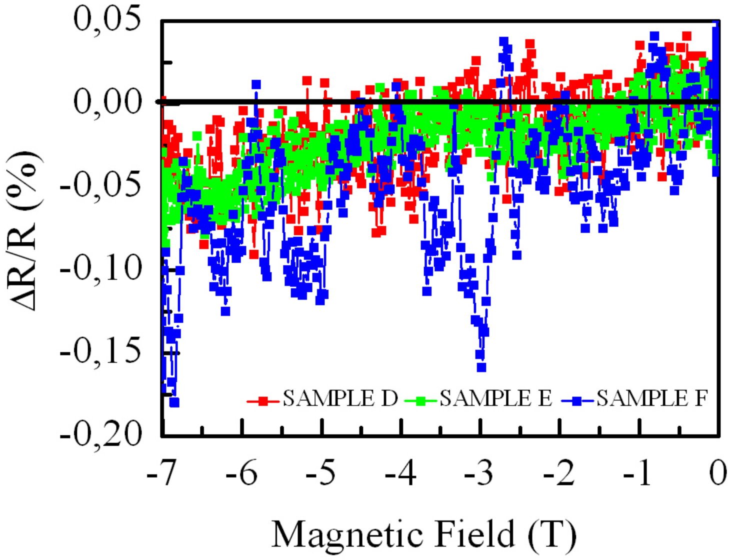

Figure 4.9: Magnetoresistance for sample D, E and F measured at room temperature.

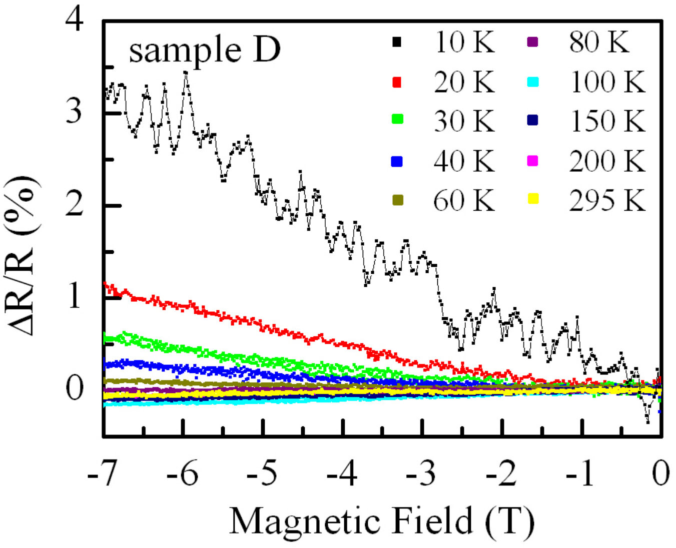

Figure 4.10: Magnetoresistance of sample D at different temperatures.

[47, 48, 62] while the change of sign is probably related to the crossover between different regimes of charge transport, as previously discussed.

The magnetoresistance intensity strongly depends on temperature. Figure

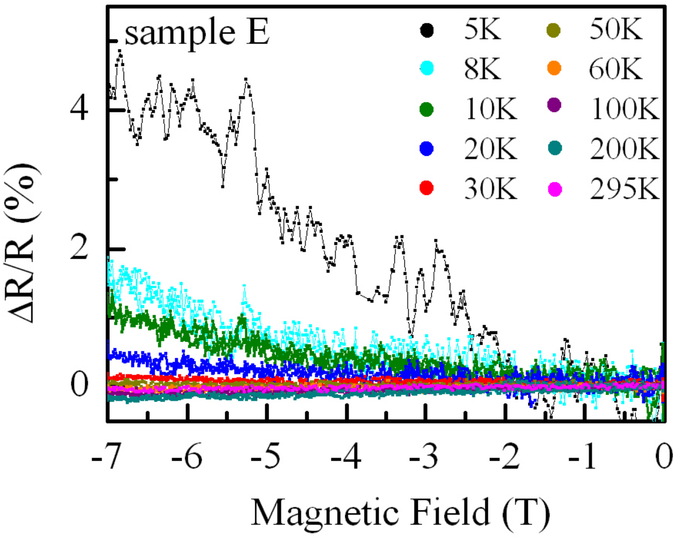

Figure 4.11: Magnetoresistance of sample E at different temperatures.

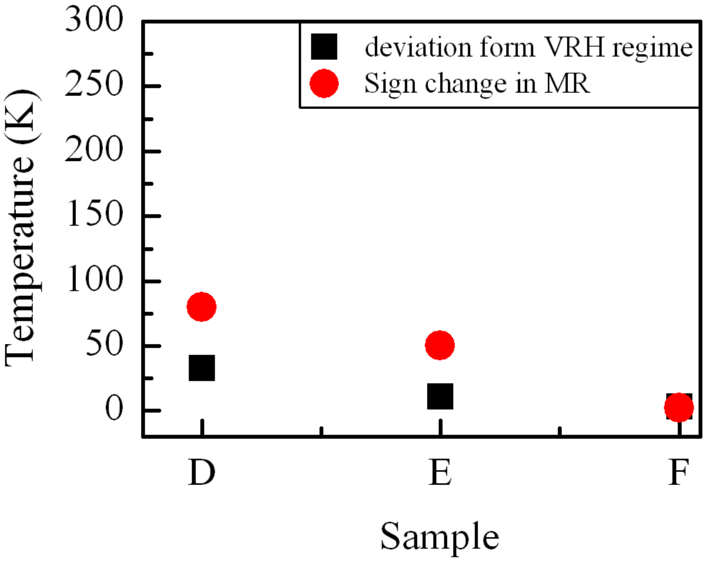

Figure 4.12: Comparison between the temperature at which we report deviation from the 2D Mott VRH transport model and the temprature at which we assist to a sign change in the magnetoresistance, for sample D, E and F.

4.13 shows the ΔR/R as a function of the applied magnetic field for sample F (T_A = 940°C) at different temperatures, down to 2 K. The magnetoresistance of the rGO film does not show any saturation up to 7 T and the intensity reaches ΔR/R = ∼64% at 2 K and 7 T, which is a surprisingly high value for a nominally non magnetic material.

Possible sources of the negative magnetoresistance are weak localization, dominance of (bi-)polaronic mechanism [63, 64] and scattering from localized magnetic moments originated from vacancies and impurities [47]. The contribution of the negative magnetoresistance due to weak localization and (bi-)polaronic mechanism is expected to saturate at relative low magnetic fields (typically <1 T) and it should vanish for temperatures above 100 K [50].

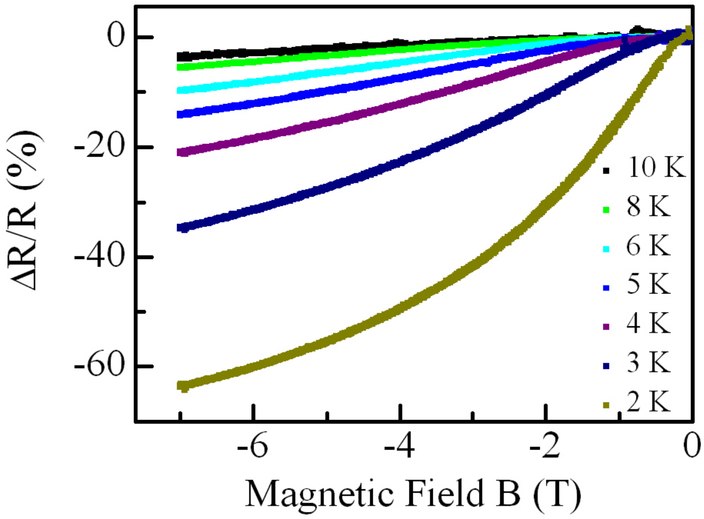

Figure 4.13: Magnetoresistance of sample F at different temperatures.

This is not the case in our measurements, thus weak localization processes can be ruled out and contribution due to the scattering with the localized magnetic moments originated from disorder, defects and impurities should be considered as the main source of high and negative magnetoresistance [47].

There is a lively literature about the influence of defects such as adatoms or vacancies on the magnetic properties of graphene-like materials. After this effect was predicted theoretically by several works [65, 66, 67], it has also been reported experimentally by a number of groups in different carbon

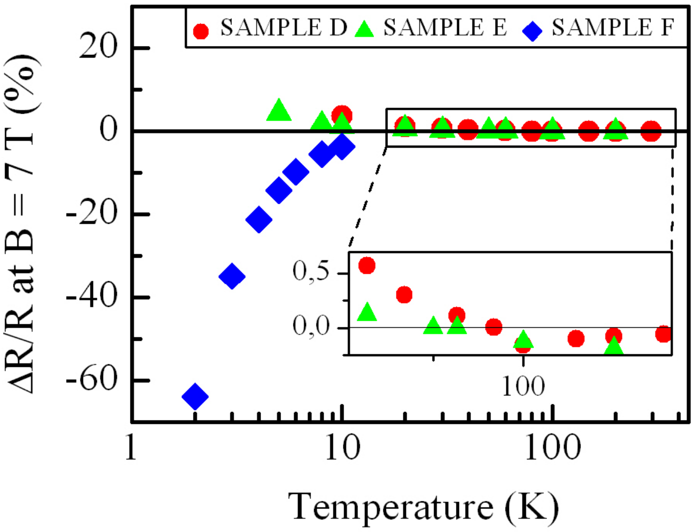

Figure 4.14: the intensity of magnetoresistance at B = 7 T for sample D, E and F as a function of temperature. For sample D and sample E we see a crossover from negative to positive magnetoresistance lowering the temperature (Inset: zoom in on the interested region), while for sample F, the magnetoresistance is always negative.

systems [62, 68, 69, 70, 71]. As discussed above, rGO does not fully recover the perfect graphene structure, but many defects remain in the final lattice after the reduction. These impurities/defects likely generate localized magnetic moments. Given the large number of these defects, it is therefore not surprising to observe their contribution to the magnetoresistance.

To gain greater insight on the origin of the magnetoresistance, we measured also the dependence of the resistance on the magnetic field applied parallel to the rGO film plane. In figure 4.15 we present ΔR/R for another sample (sample G, for which T_A = 900°C). The magnetoresistance measured at T = 8 K with the magnetic field B applied parallel to the GO film plane results to be almost identical to the one measured with the field perpendicular to the sample plane. This lack of anisotropy excludes possible orbital origins, such as localization, further corroborating our suspect on localized magnetic moments as the main source of the observed magnetoresistance. Also, to exclude any possible contribution due to any eventual magnetic phase of Cr,

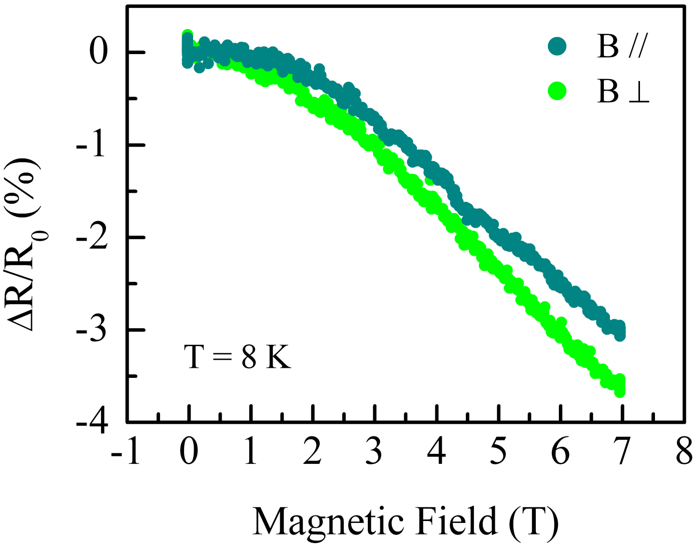

Figure 4.15: $\Delta R/R$ in four probe configuration of sample G (T_A = 900°C) at T = 8 K. Dark green corresponds to magnetic field parallel to rGO plane, while light green indicates magnetic field perpendicular to rGO plane.

which is used in the fabrication process of the electrical contacts, samples with Pd contacts were measured, finding similar results.

Very recently Qin and coworkers [62] showed non-saturating negative magnetoresistance in 110 layers of GO films reduced by annealing at 600°C. They observed $\Delta R/R$ up to ~2.5% at 5 K and 1 T, claiming that the origin is due to spin dependent scattering of defects. This value is consistent with our results, but they also report minor hysteresis loops in their magnetoresistance measurements which we did not observe. Sometimes hysteresis loops depend on the sweeping rate of the field; our measurements are performed at 200 Oe/s but also control tests have been done using different speeds as 50 Oe/s and 100 Oe/s, without finding any hysteresis.

4.5 Flake size dependence

The second part of this chapter deals with the investigation of the dependence of charge carrier transport on the size of the flakes that compose the thin films.

The study is carried out as follows: three different solutions have been prepared with the method exposed in section 2.1. By changing the sonication time, it is possible to achieve different flake sizes, as mentioned in chapter 1. We demonstrated by XPS measurements that the oxidation level of the three different solutions is the same, so that they differ from each other only by the average lateral dimensions of the flakes and not by chemical composition. The same thermal treatments has been done in order to reduce the deposited films at three different levels. Then, measurements of resistance as a function of temperature, from room temperature down to 2 K, and as a function of an external magnetic field up to 7 T have been done to study the charge carried transport and the magnetotransport in these samples.

4.5.1 Sample characteristics

The set of samples analyzed is fabricated as described in chapter 2.

The solutions have been sonicated respectively for 2 hours (S2), and for 20 hours (S3); a set of samples come from non-sonicated pristine GO solution (S1).

To control the resulting flake sizes, we diluted the solutions of GO in distilled water until we reached single flake deposition on Si/SiO_2 substrate (dilution 1:8). The samples were then annealed at 400°C in high vacuum for 1 h to enhance contrast for scanning electron microscopy (SEM) imaging.

Figures 4.16, 4.17 and 4.18 show SEM images of the GO depositions with different size distributions.

As it typically occurs for random processes as the fragmentation due to sonication, GO solutions are characterized by flakes having lateral dimensions that span various order of magnitudes. This means that pristine GO suspension S1, with very large flakes, also hosts sub -100 nm flakes, while, on the other hand, strongly sonicated S3 solution may contains flakes in the

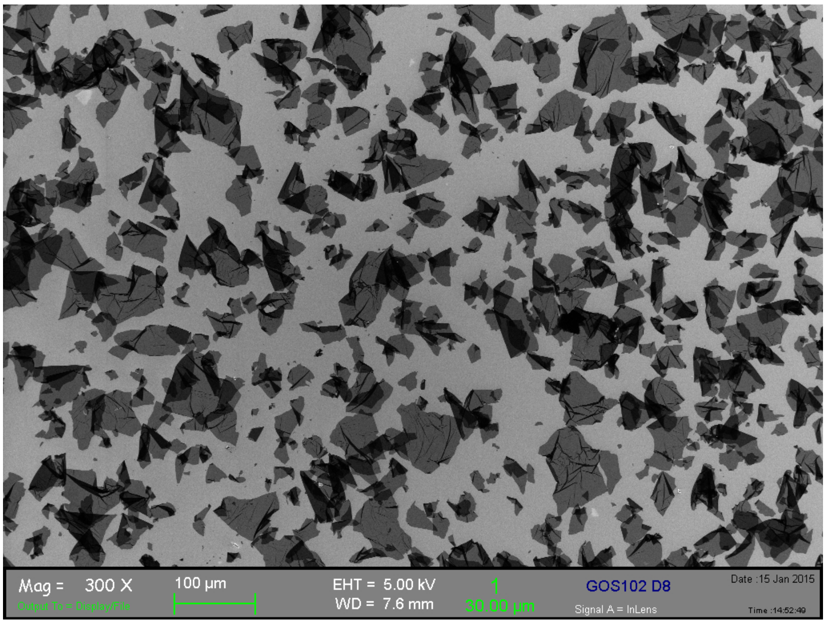

Figure 4.16: SEM imaging of GO solution S1, sonication time 0 hours. Magnification 300X.

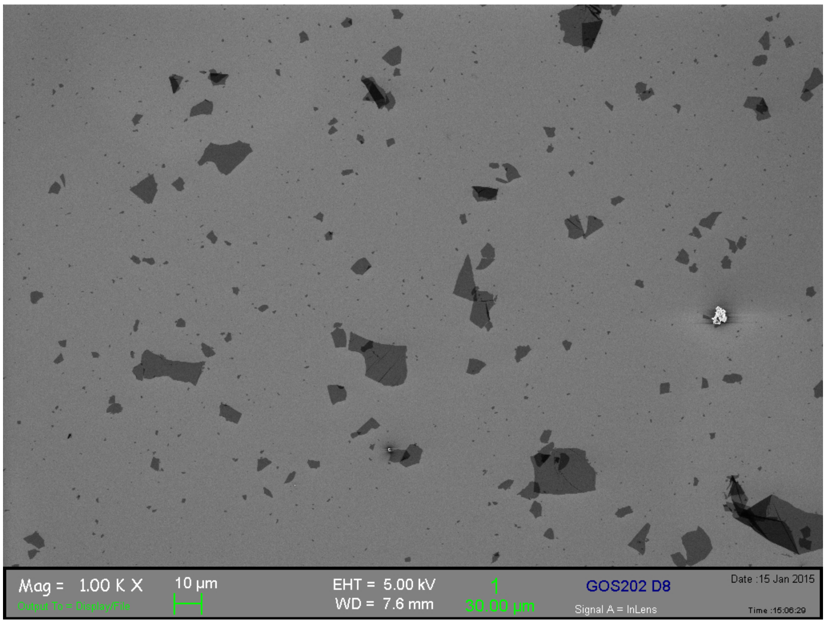

Figure 4.17: SEM imaging of GO solution S2, sonication time 2 hours. Magnification 1000X.

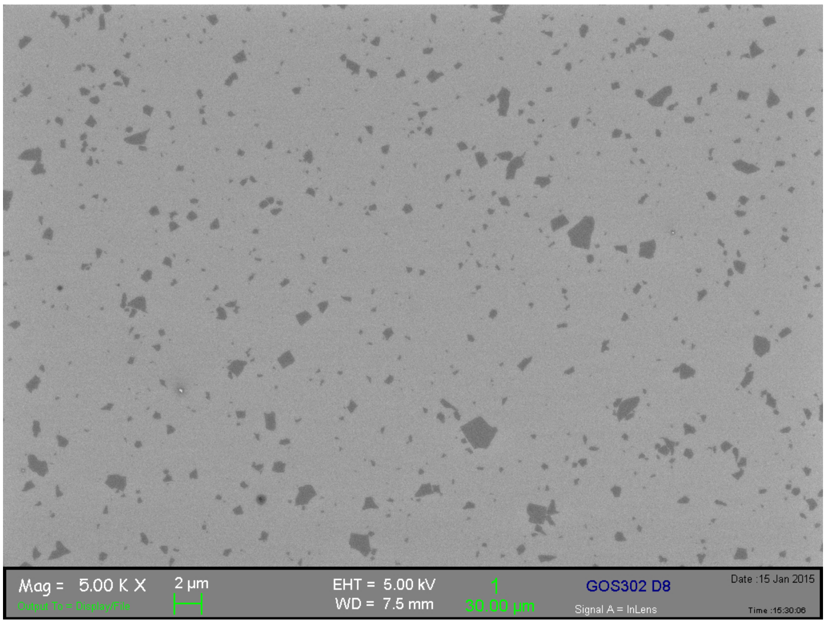

Figure 4.18: SEM imaging of GO solution S3, sonication time 20 hours. Magnification 5000X.

μm range size.

Figure 4.19 presents the lateral size distributions for the three solutions from SEM images.

The resulting average size of the flakes is 20-30μm for solution S1, 1-2μm for solution S2 and 200nm for solution S3.

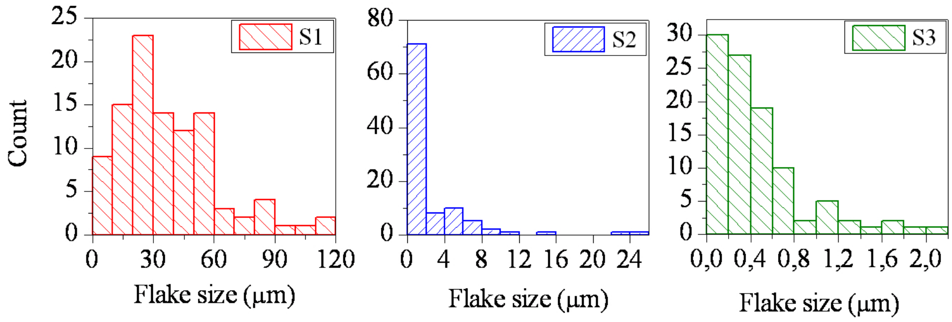

Figure 4.19: Lateral size distributions of the GO flakes for the three solutions S1, S2 and S3.

The three solutions have been deposited on Si/SiO$_2$ 300 nm substrate with the same recipe.

AFM morphological characterization of the films shows that non sonicated solution S1 forms thicker films with the presence of huge wrinkles and substructures (figure 4.20), while most sonicated solution S2 and S3 produces smoother and thinner films (ref. to figure 3.2 for comparison and to ref. [72]).

To control the final thickness of the deposited films, a rectangular shape

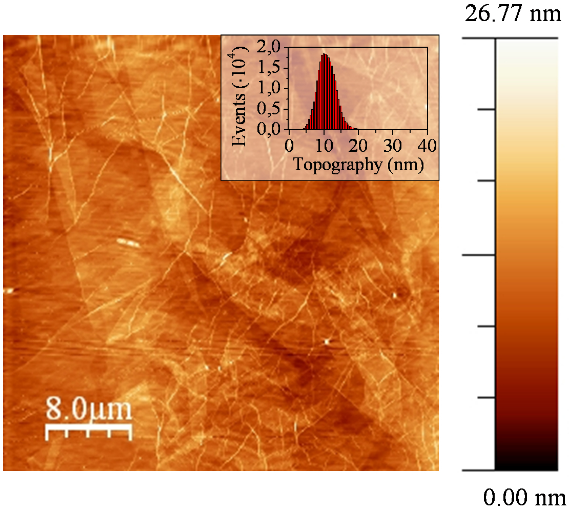

Figure 4.20: AFM images of 15 nm thick film of GO deposited by spin coating from non-sonicated GO solution S1 (larger flakes).

has been patterned with the EBL on the substrate, then GO solution has been deposited by spin coating and, after the lift-off procedure, the profile has been measured with the profilometer.

The resulting thickness is ∼15 nm for solution S1, ∼10 nm for solution S2 and ∼7 nm for solution S3.

The samples from each solution have been thermally reduced in high vacuum (10^{-6} mbar) for one hour at 300°C, 600°C and 900°C.

In table 4.2 are summarized the characteristics of the measured samples.

GO Solution	Flake size	T_A (°C)	Sample Name
S1 (pristine)	∼20μm	300	S1a
		600	S1b
		900	S1c
S2 (2h sonication)	∼2μm	300	S2a
		600	S2b
		900	S2c
S3 (20h sonication)	∼200nm	300	S3a
		600	S3b
		900	S3c

Table 4.2: Characteristics of samples from different solution of GO.

4.5.2 XPS analysis

X-ray photoelectron spectroscopy (XPS) has been used to control the oxidation state of the GO and rGO films in order to make sure that different sonication and successive thermal annealing do not lead to different chemical composition among the three used solutions.

XPS characterization has been carried out by PhD student A. Kovtun at the ISOF Institute of the CNR of Bologna.

Figure 4.21 shows the XPS spectra of pristine GO films obtained from solution S1 and solution S3, with the relative deconvolution in the typical contributions: sp^2-hybridized carbon, sp^3-hybridized carbon, and the main functionalities C-O-C and O=C-O.

The two spectra were identical (within the experimental error), so that there is a negligible difference in the oxidation state of the two solutions. This ensures that the fragmentation due to sonication only acts on the final lateral dimension of the flakes leaving unmodified the chemical composition.

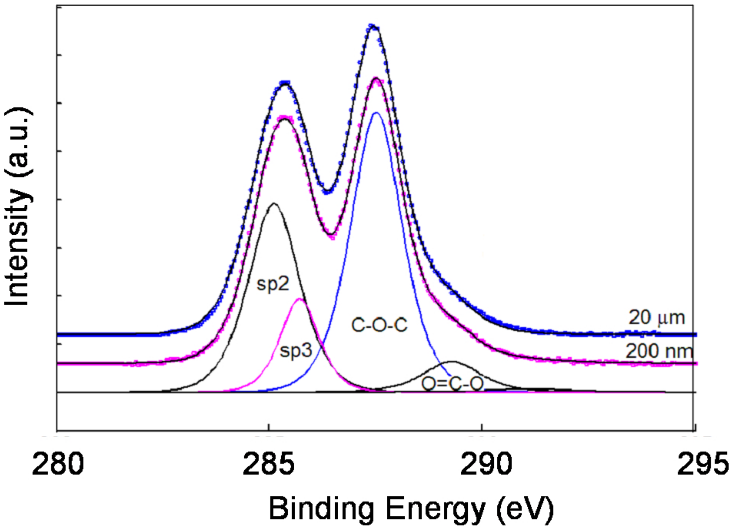

Figure 4.21: XPS spectra of pristine GO films deposited from solution S1 (blue line) and solution S3 (pink line), with the relative deconvolution.

To be sure that also the reduction through thermal annealing leads to the same oxidation level in all the three different solutions, and therefore the efficiency is not affected by the size of the flakes that compose the films, we acquired XPS for all the nine samples after the thermal treatment.

Figure 4.22 reports the nine curves of the spectra of the reduced GO films: no significant difference is visible among S1, S2 and S3 annealed at the same temperature, so that again we have the same chemical composition for the three solutions for each step of reduction. The prominent peak is due to sp^2-hybridized carbon atoms while the successive hump, related to the oxygen-containing functional groups, scales correctly with the annealing temperature.

From the fits of the XPS spectra and the analysis of the C 1s components, it has been possible to estimate the C/O ratio (figure 4.23). The value scales correctly with the annealing temperature, as the reduction proceeds, and was independent from the lateral dimension of the flakes, going from ∼4.5 for samples annealed at 300°C to ∼11.5 for samples annealed at 900 °C. This shows that the flake size does not affect the chemistry of the thermal

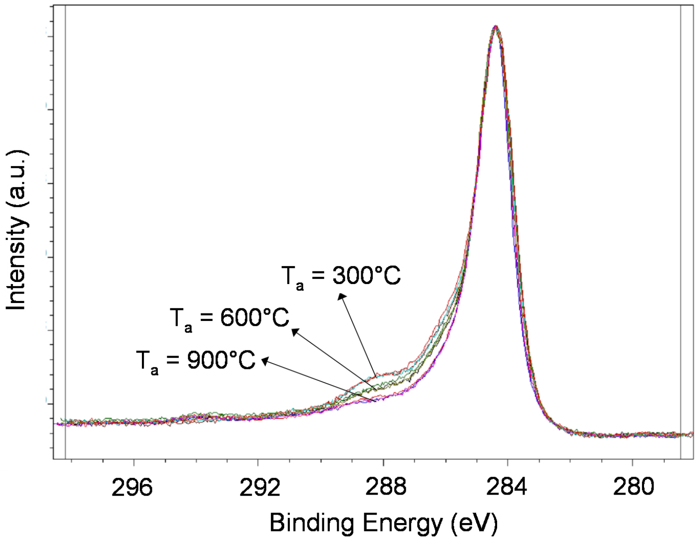

Figure 4.22: XPS spectra of the analyzed samples annealed at 300°C, 600°C and 900°C.

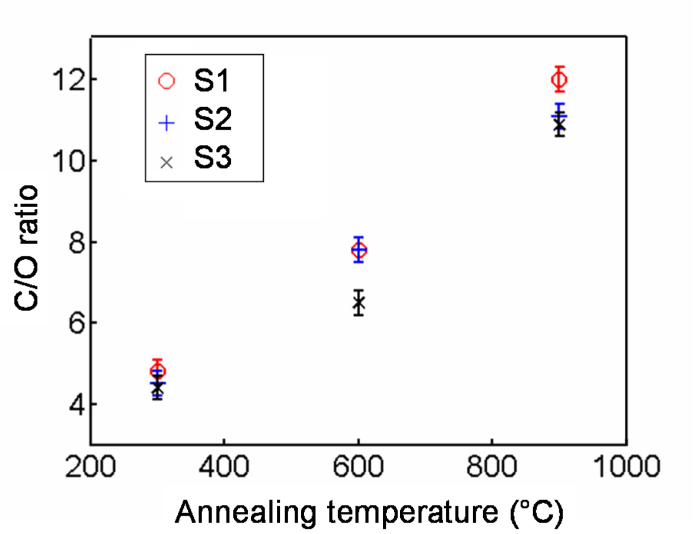

Figure 4.23: C/O ratio as a function of the annealing temperature for the three solutions S1, S2 and S3.

reduction.

4.5.3 Low temperature resistance measurements

To investigate the charge transport dependence on the flake dimensions, we measured the resistance as a function of the temperature R(T), from room temperature down to 2 K.

At all the annealing temperatures, we report different room temperature resistance for the three different solutions. In fact, the R_{300K} scales with the size of the flakes, being lower for samples with larger flakes.

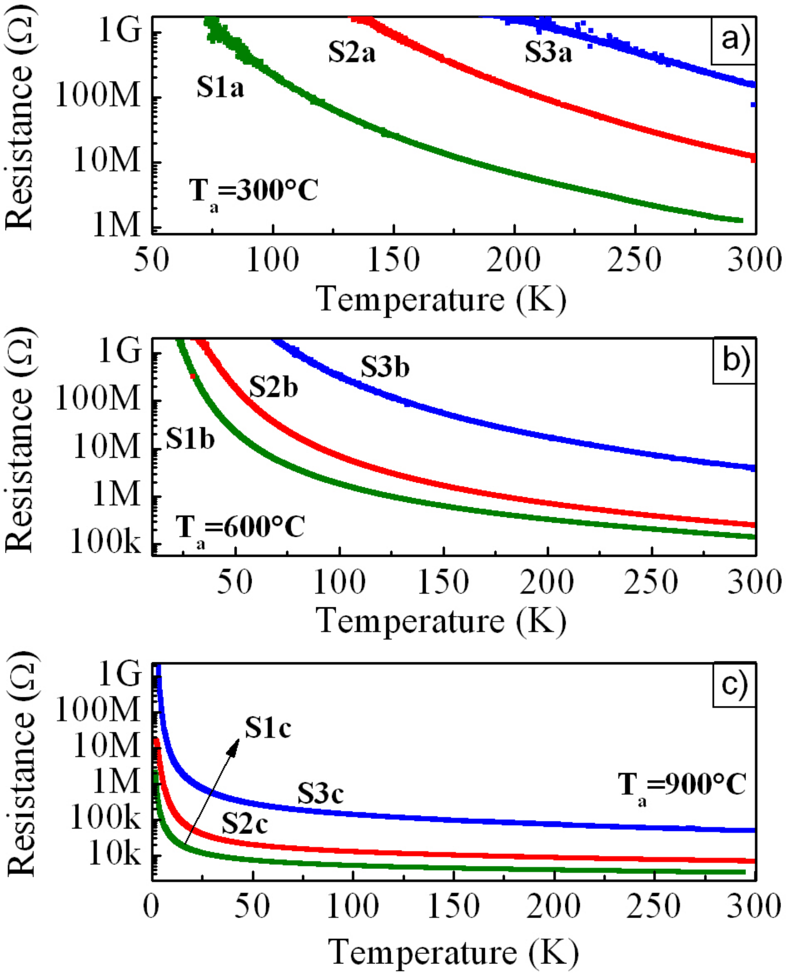

Figure 4.24: Resistance as a function of the temperature for a) samples annealed at 300°C, b) samples annealed at 600°C and c) samples annealed at 900°C.

R(T) curves increase up to 5 orders of magnitude by lowering the temperature (figure 4.24). The slopes of the curves, at each annealing temperature, scales with the size of the flakes, increasing faster by decreasing lateral dimensions of the flakes.

We analyzed the data in the same framework used in the previous sections, i.e. the 2D Mott Variable Range Hopping transport model.

The behavior of the resistance has been analyzed by plotting R in a semi-log plot as a function of $1/T^{1/3}$ (figure 4.25).

Interestingly, at each annealing temperature, the slopes of the linear fits

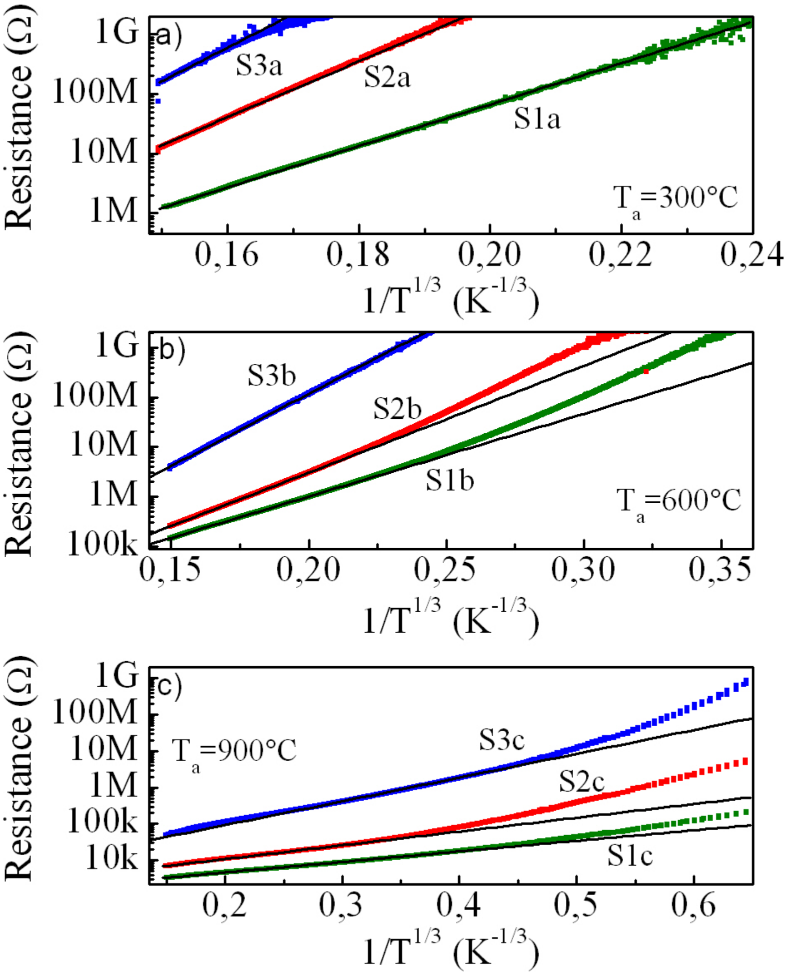

Figure 4.25: Resistance as a function of $T^{-1/3}$ for a) samples annealed at 300°C, b) samples annealed at 600°C and c) samples annealed at 900°C, with relative fits to 2D Mott variable range hopping (black lines).

scale with the lateral dimension of the flakes.

From the fits to the 2D Mott VRH, it was possible to calculate the characteristic temperature T_0, which for each solution increases with increasing the annealing temperature (as already reported in section 4.3), and at the same time, for each annealing temperature, scales with the lateral dimension of the flakes, being smaller for larger flakes (see figure 4.26).

Also for these samples, we report clear deviations from the 2D Mott Variable

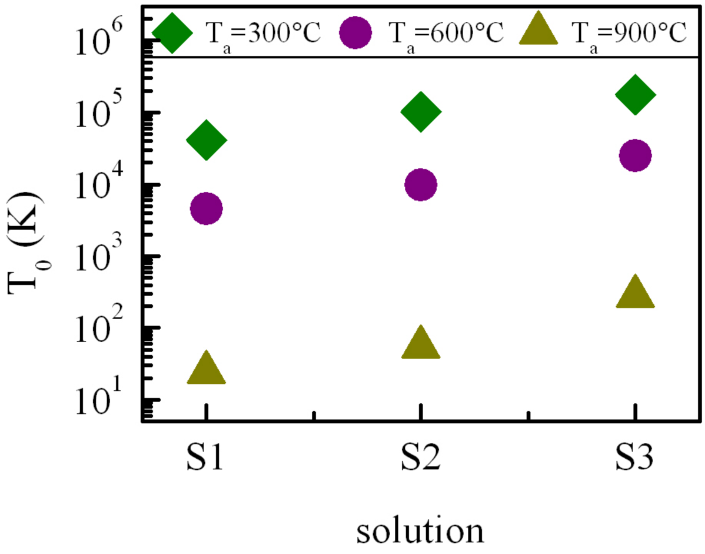

Figure 4.26: Semi-log plot of the characteristic temperature T_0 as a function of the flake size, for each reduction step: T_a=300°C (green diamonds), T_a=600°C (purple circles) and T_a=900°C (dark yellow triangles).

Range Hopping transport model at low temperatures, as already discussed in section 4.3. In particular, we observe that for samples annealed at 300°C, the experimental data fit the $R = R_0 \cdot exp(T_0/T)^{1/3}$ law for all the temperature range, while for samples annealed at 600°C and 900°C there is a critical temperature T_c at which the resistance increases faster than the model's law. Again, we can suppose that at this temperature a crossover to another regime occurs, due to the modifications of the characteristic lengths of the disordered systems caused by the lowering of the temperature.

Still, at each annealing temperature, we observe a clear scaling of the slope of the 2D Mott VRH fits with the size of the flakes. This suggests a gain in the electrical conductivity with increasing dimensions of the flakes. Since the oxidation state is the same for the three solutions at each reduction step (as previously discussed from XPS measurements), one may exclude that the behavior of the resistance is due to a scaling of the defect density (at the same annealing temperature). Instead, it is likely that the conductivity is dominated by the number of junctions that a charge flowing between the electrodes meets, promoting electrical conductivity in films with larger flakes. Since the oxidation state is the same for the three solutions at each reduction step (as previously discussed from XPS measurements), one may exclude that the behavior of the resistance is due to a scaling of the defect density (at the same annealing temperature). Instead, it may be dominated by the number of junctions that a charge flowing between the electrodes meets, concluding that the electrical conductivity is promoted in films with larger flakes.

4.5.4 Magnetotransport

We also investigated the behavior of the resistance under an applied magnetic field as a function of the flake size, to see if also the magnetotransport is affected by the lateral dimensions of the flakes.

Samples annealed at 300°C and 600°C, i.e. samples S1a, S2a, S3a, S1b, S2b and S3b, were too resistive and their magnetoresistance $\Delta R/R$, if any, was within the electrical noise. We therefore report only data from samples S1c, S2c and S3c ($T_A = 900$°C).

The three samples show negative magnetoresistance from 300 K down to the lowest temperature. The shape and the behavior of the magnetoresistance as a function of the temperature is very similar for the three samples; as an example we report $\Delta R/R$ curves for sample S1c in figure 4.27.

The magnetoresistance of the rGO films does not show any saturation up to 7 T, and the intensity reaches several tens percents at 2 K (see figure 4.28). For sample S3c is has been possible to measure only down to 8 K, because at lower temperature it became too resistive.

The absolute value of the intensity of the magnetoresistance may vary of few

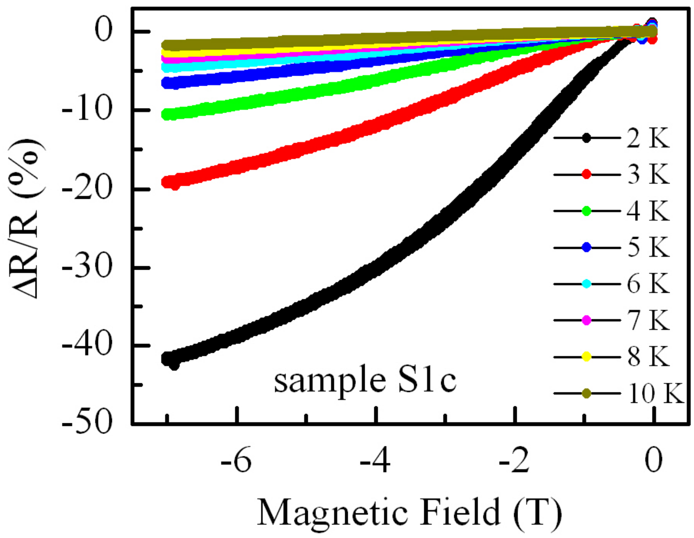

Figure 4.27: Magnetoresistance $\Delta R/R$ of sample S1c at different temperatures.

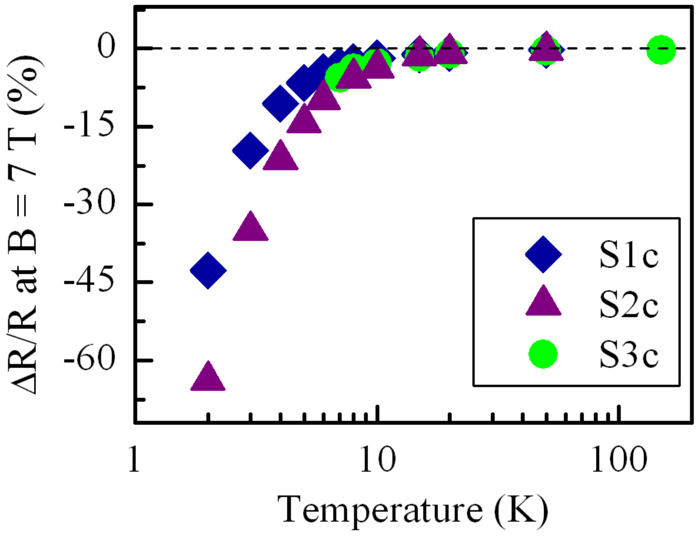

Figure 4.28: Intensity of magnetoresistance $\Delta R/R$ at B = 7 T for sample S1c, S2c and S3c as a function of temperature.

percents depending on the aging of the sample (in particular with the time passed after the annealing), the absolute value of the starting resistance, the contact resistance and so on. So we observe no physical difference between the behavior of the magnetoresistances of the three samples, since little differences in the intensity lay within the statistical error.

We may conclude that the size of the flakes does not affect the magnetotransport, which is then more a local effect. This further corroborates the hypothesis already discussed in section 4.4 that such a high and negative magnetoresistance is due to scattering with magnetic moments originated from disorder, defects and impurities.

4.6 Qualitative model for charge transport in rGO films

We want to here summarize the main results obtained by proposing a qualitative model for charge transport in rGO films as a function of temperature and magnetic field.

The model is sketched in figure 4.29. rGO films are characterized by graphitic domains surrounded by a sp^3-hybridized matrix. At room temperature, charge carrier transport occurs via hopping through the graphitic domains, while when flowing within a single domain, the charge experiences spin flip at the magnetic moments originated from defects and vacancies, which are present in the graphitic lattice (panel a of figure 4.29).

By lowering the temperature, electrons become more and more localized and the resistance increases (figure 4.29b). As the temperature is low enough, the system may even change the charge transport regime due to a modification of its characteristic lengths.

When an external magnetic field is applied at high temperatures, the paramagnetic moments present within a domain align with the external field, so that the spin flip scattering is reduced. Here we observe a decrease of the resistance as a function of the strength of the magnetic field, and thus to a negative magnetoresistance, as reported for all of our samples (figure 4.29c).

If the temperature is now decreased, and the electrons are more localized, orbital effects are enhanced, and the presence of an external magnetic field

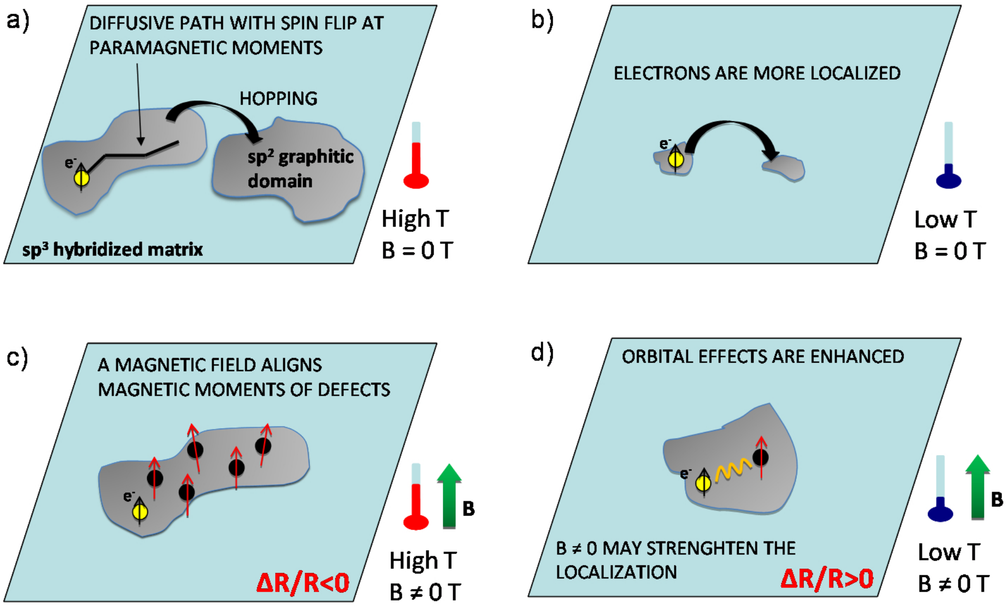

Figure 4.29: Sketch of a qualitative model for the electrical transport in rGO films as a function of temperature and external magnetic field.

may lead to a strengthening of the localization and thus to and increase of the resistance. If we are in this condition, positive magnetoresistance appears, as reported for intermediate level of reduction of the GO films (section 4.4) for which the defect density is still very high (figure 4.29 panel d). But if the graphitic domains are large enough, the system could always remain in the previous conditions and even at very low temperatures, down to 2 K, it would present negative magnetoresistance, as we observed for all the most reduced samples ($T_A \geq 900°C$).

4.7 Conclusions

In this chapter we characterized the electrical and magnetic transport properties of rGO films at intermediate reduction degrees and in a wide temperature range (2 - 300 K).

The room temperature resistance of rGO films scales with the annealing temperature, although for very high treatment temperatures ($\geq 700°C$) the gain in the level of reduction is limited, likely by the increase of topological defects and structural disorder induced by the treatment itself.

The temperature dependence of the resistance fits the law $R = R_0 exp(T_0/T)^{1/3}$ for temperatures well below the liquid nitrogen temperature, consistently with 2D Mott-VRH for all the intermediate level of reduction. The slopes of the linear fits to the model scale with the annealing temperature, indicating clearly a gain in the electrical conductivity due to a decrease of defect density and the restoration of the conjugated structure. At lower temperatures, a crossover to another regime likely occurs.

Moreover, we investigated the electrical transport under an applied magnetic field, finding high magnetoresistance values at low temperatures. Since we do not see saturation up to B = 7 T and magnetoresistance signal has been measured at all the temperature, we had to rule out all the possible mechanisms for the origin of the observed magnetoresistance, leaving only the contribution due to scattering from magnetic moments originated from defects and vacancies.

In the second part of the chapter, we investigated the dependence of the electrical transport by the size of the flakes that form the thin films.

We firstly characterized morphologically the films deposited from the three solutions used. XPS analysis demonstrated that the chemical composition and the oxidation state is independent from the flakes size, both in pristine GO films and in thermally reduced rGO films. It was also possible to calculate the C/O ratio of the reduced films, finding values from ∼4.4 for T_A=300°C to ∼11.5 for T_A=900°C.

We then investigated the charge transport dependence on the flakes size by resistance measurements as a function of temperature, from room temperature down to 2 K. Both the room temperature resistance and the slope of the R(T) curves scale with the flake size, suggesting that the electrical transport is favored in films composed by larger flakes.

Magnetotransport in these samples was independent from the flakes lateral dimensions, indicating that the origin of the measured magnetoresistance is more of a local effect.

We finally proposed a qualitative model to sum up all these results, which is

presented in the last section of this chapter.
These results extend the temperature and magnetic field range of previous works and highlight the interplay of different mechanisms of charge transport in rGO thin films.

Chapter 5

GO-based devices in spin-valve geometry

Carbon-based materials are promising candidates for the development of spintronic devices: thanks to their weak spin-orbit interaction and hyperfine interaction they present long spin-relaxation lifetime, which allows spin manipulation [73, 74, 75, 76, 77].

Graphene and graphene-related materials also attracted interest in this field and spin transport properties started to be investigated.

Indeed, long spin diffusion length of about a few micrometers have been reported in graphene-based devices using both two and four terminal geometries [78, 79]. Moreover, several groups have demonstrated graphene lateral spin-valve structures with long spin lifetimes and diffusion lengths [79, 80].

The introduction of GO in this field is very attractive, due to its wide processability, the tunability of its optical and electronic properties (as discussed in the previous chapters) and the possibility of easy chemical functionalization.

In this chapter is presented a vertical spin valve device, where a rGO layer is sandwiched between $La_{0.7}Sr_{0.3}MnO_3$ (LSMO) and Co ferromagnetic electrodes. LSMO is an half-metallic oxide ferromagnetic material which exhibits nearly 100 % spin polarization at low temperature, and unlike other ferromagnetic materials, such as some metals, it is very stable in ambient conditions. Devices based on these electrode materials, with organic semiconductor as spacing layer, show a giant magnetoresistance (GMR), which is usually ascribed to the injection and transport of spin-polarized currents between the two electrodes [81, 74, 75, 82, 83, 84].

After a brief presentation of the fabrication process of these LSMO/GO/Co vertical devices, preliminary results on the low temperature characterization of spin valve effect, from room temperature down to 100 K, and the voltage bias dependence at 100 K, are reported.

This project has been developed in collaboration with the group of Dott. V.A. Dediu of the ISMN Institute of the CNR of Bologna.

5.1 Fabrication of LSMO/GO/Co vertical devices

The bottom 15 nm thick LSMO electrode was grown by channel spark ablation (CSA) by the group of Dott. V.A. Dediu of the ISMN Institute of the CNR of Bologna on $SrTiO_3$ substrate, in strip shape with lateral dimension of 1 mm using shadow masks. Then, a rectangular shape has been patterned with standard EBL technique and a layer of 180 nm thick GO has been deposited by spin coating. Finally, the top electrode consisting of a strip-shaped 20 nm thick and 100 μm large Co film has been evaporated by an electron-gun.

Electrical contacts are provided by gold wires fixed to the sample with indium thin slices which sticks to the Co and LSMO electrodes by simple pressing.

In figure 5.1 is scketched the typical vertical configuration of a LSMO/GO/Co device.

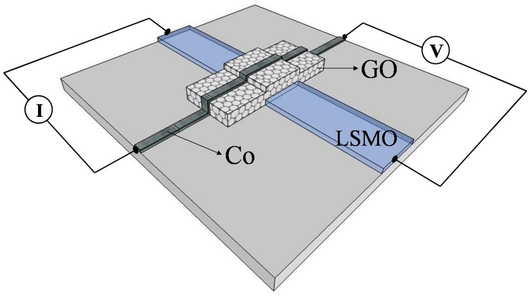

Figure 5.1: Scketch of a vertical LSMO/GO/Co device, with relative electrical connections for the characterization.

5.2 Devices characterization and measurement setup

After the deposition of GO on the LSMO strip, AFM imagining has been used to characterize morphologically the device, and to measure the GO thickness.

AFM analysis was performed at the Scanning Probes Microscopy Lab of the CIGS Center of the University of Modena and Reggio Emilia.

Figure 5.2 shows an AFM image where the GO film on the left is on top of the LSMO bottom electrode, on the right. The LSMO film presents some typical round-shaped structures which come from the deposition process, while the GO film also shows a greater roughness than the one measured when it is deposited on top of Si/SiO_2 substrate: the RMS roughness value is 9.9 nm (analysis carried out with WSxM 5.0 software, see figure 5.3 for the heights histogram).

AFM profiles analysis and profilometer measurements show that the average thickness of the GO film on top of the LSMO strip is $\sim$180 μm.

The samples are placed in a cryostat and 4-probes measurements are performed down to liquid nitrogen temperature at the ISMN Institute of the CNR of Bologna.

The input bias voltage V is applied between one side of the LSMO bottom electrode and one side of the top Co electrode. The corresponding current I is measured at the remaining two extremities (see picture 5.1) of the elec-

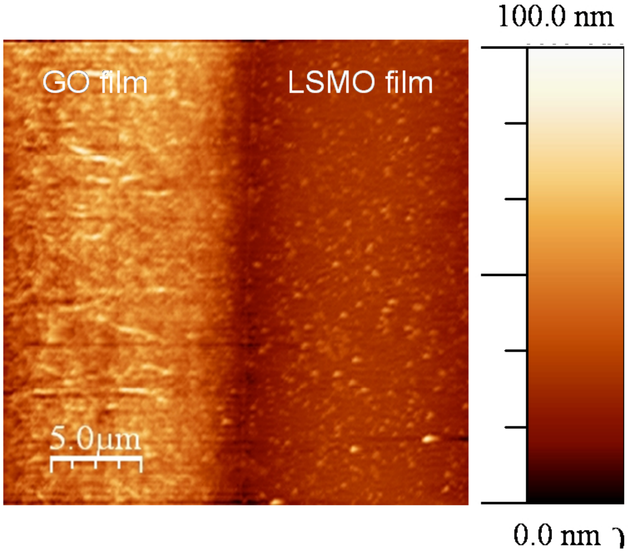

Figure 5.2: AFM image showing on the left the GO film and on the right the LSMO bottom electrode.

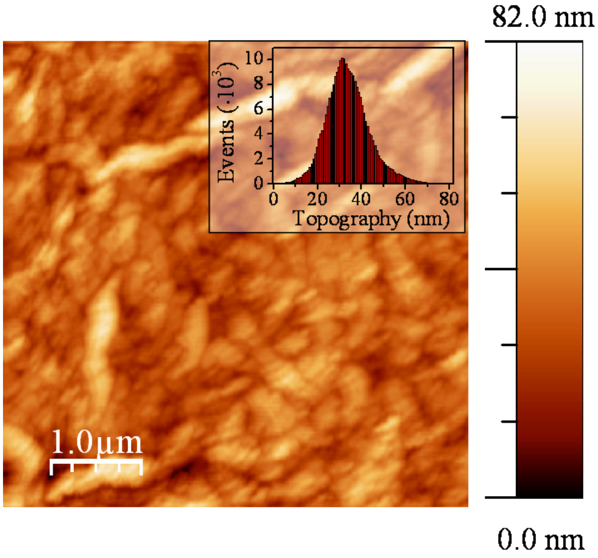

Figure 5.3: AFM image showing the GO film deposited on the LSMO electrode, with relative heights histogram.

trodes. The resistance of the device is then defined as R = V / I .

Since LSMO ferromagnetic electrode and Co ferromagnetic electrode show different coercive magnetization fields, it is possible to change the magnetization alignments of the two electrodes from parallel to anti-parallel by sweeping the external magnetic field. Magnetoresistance is obtained by measuring R as a function of the applied magnetic field, oriented parallel to the device plane.

5.3 Magnetoelectrical characterization of the electrodes

The resistance of the cobalt stripe used as top electrode as a function of the temperature is shown in figure 5.4. It present a typical metallic behavior,

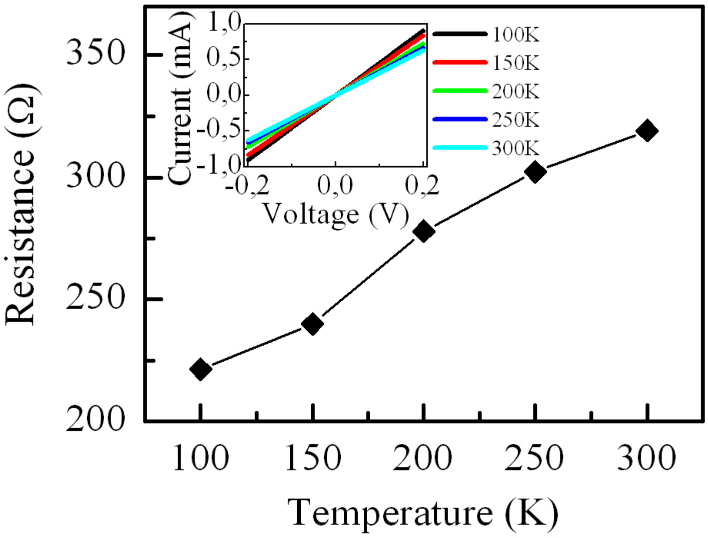

Figure 5.4: Top cobalt electrode resistance as a function of the temperature. Inset: I-V characteristic curves for each temperature step.

with a resistance going from 319 Ω at T = 300 K to R = 221.4 Ω at the lowest temperature of T = 100 K.

The magnetoresistance of the top electrode at T = 100 K is presented in figure 5.5. By sweeping the magnetic field from -3000 Oe to 3000 Oe it is

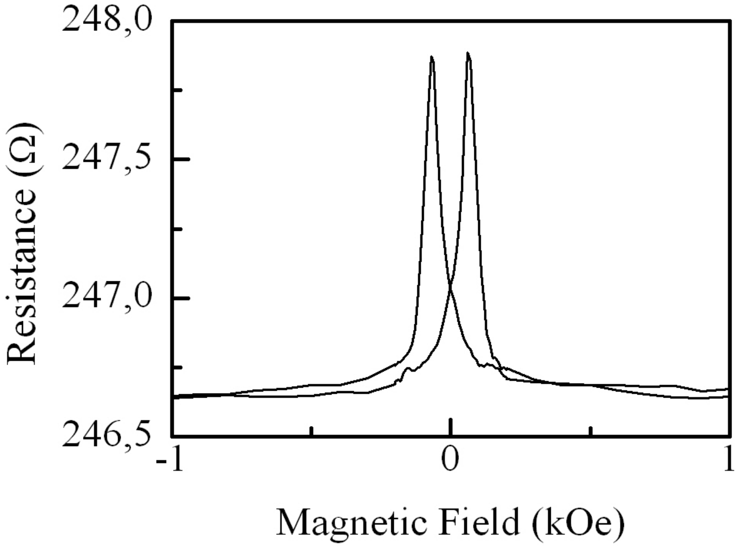

Figure 5.5: Top cobalt electrode resistance as a function of the magnetic field, at T = 100 K and V_{bias} = -100 mV.

possible to see the typical MR curve, showing the peaks in correspondence of the coercive fields of ∼65 Oe. The intensity of the MR at the lowest temperature is ∼0.52 %.

The bottom electrode was characterized in the same way: R(T) curve shown in figure 5.6 presents a typical metallic behavior, with resistance value going from 123.2 kΩ at T = 300 K to 42.9 kΩ at T = 100 K.

The magnetoresistance of the LSMO stripe is positive and reaches the intensity of 1.19% at T = 100 K (figure 5.7).

5.4 Temperature dependence and voltage bias dependence of the spin valve effect

The resistance of the device as a function of temperature is reported in figure 5.8. By lowering the temperature from room temperature down to 100 K, it exhibits metallic behavior and R decreases. I-V characteristic curves measured at each temperature step are linear in this temperature range between -200 and +200 mV, indicating ohmic conduction between the two electrodes

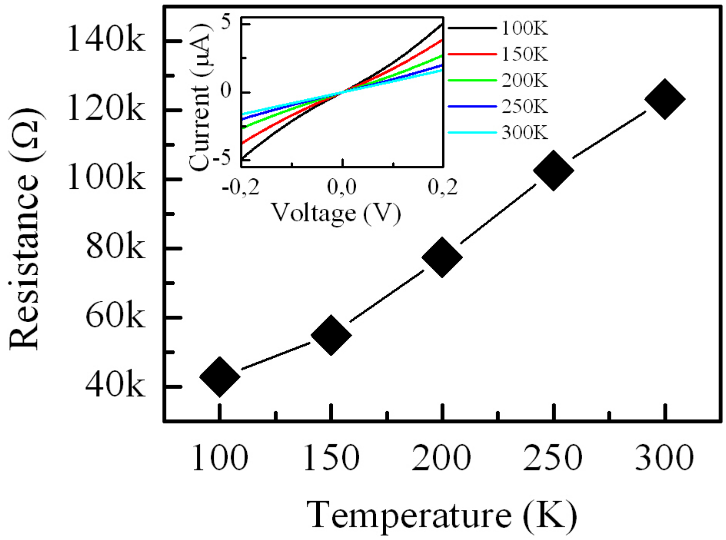

Figure 5.6: Bottom LSMO electrode resistance as a function of the temperature. Inset: I-V characteristic curves for each temperature step.

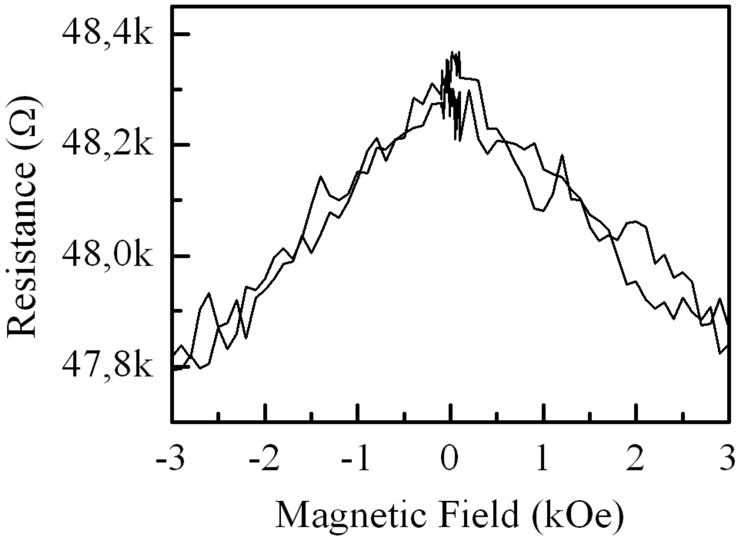

Figure 5.7: Top cobalt electrode resistance as a function of the magnetic field, at T = 100 K and V_{bias} = -100 mV.

(inset of figure 5.8).

At each temperature step, also the resistance of the device as a function of

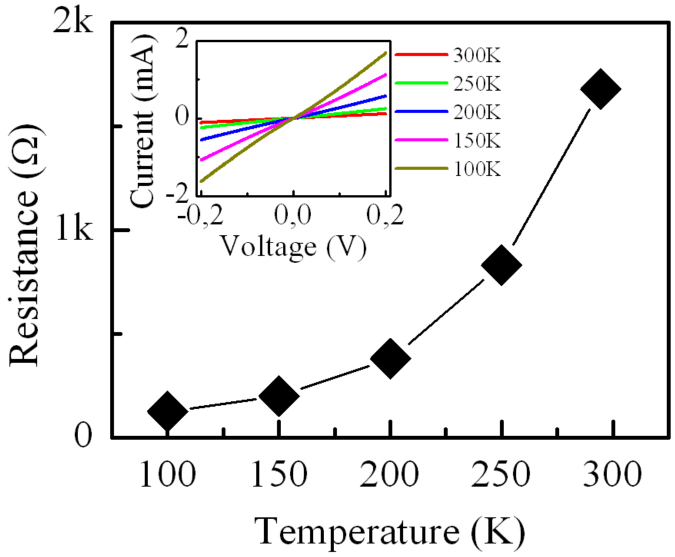

Figure 5.8: Device resistance as a function of the temperature. Inset: I-V characteristic curves for each temperature step.

the applied in-plane magnetic field has been measured. At room temperature and at T = 250 K, the behavior of the resistance follows the magnetoresistance of the bottom electrode, showing a typical MR curve for LSMO thin film. By lowering the temperature, instead, inverse magnetoresistance effect starts to appear. The curves clearly show resistance dips corresponding to the electrodes being in the antiparallel orientation, while the high resistance state corresponds to the electrodes being oriented parallel to each other (figure 5.9 panel a).

The MR intensity in percent is defined by the expression MR (%) = 100 $\cdot(R_{AP} - R_P)/R_P$, where R_{AP} and R_P are the resistance of the anti-parallel and parallel magnetization configuration of two electrodes, respectively.
The panel b) of the figure 5.9 shows that the intensity of the MR signal of our device increases with decreasing temperature, reaching the absolute value of 2.3% at the lowest temperature T = 100 K (figure 5.9 a).
This inverse MR effect is well accounted for devices with organic semiconductor as Alq$_3$ as spacing layer between the two LSMO and Co electrodes, although its explanation was proposed only recently [85].

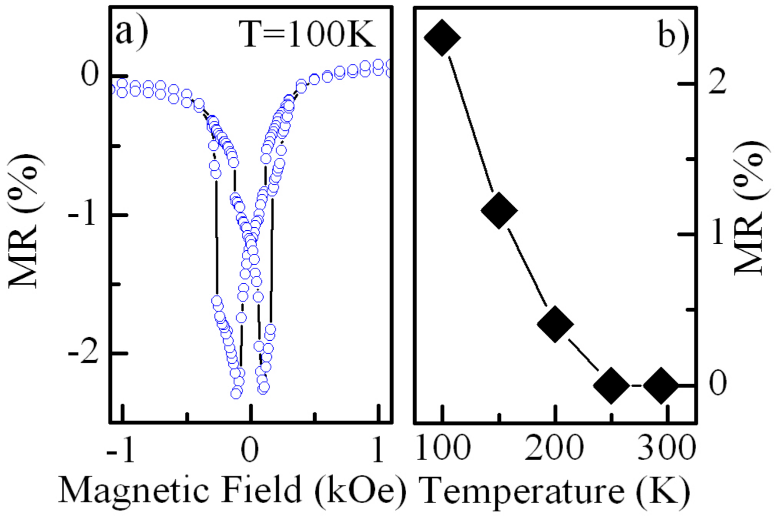

Figure 5.9: a) Device resistance as a function of the in-plane applied magnetic field measured at V_{bias} = -100 and T = 100 K. Panel b) shows the intensity of the spin valve effect as a function of the temperature.

Moreover, the intensity of the MR effect detected in such devices scales

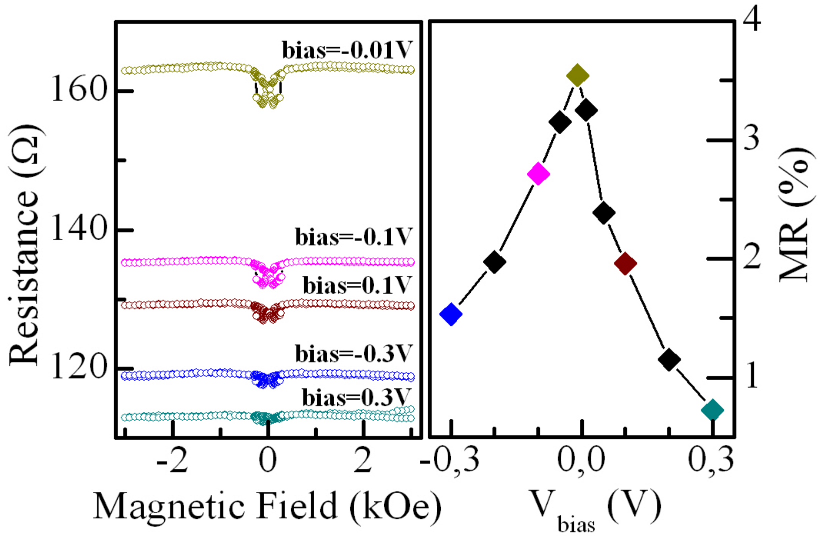

Figure 5.10: Left: MR curves at different voltage bias, measured at T = 100 K. Right: MR intensity as a function of the voltage bias, at T = 100 K.

with the absolute bias voltage value. Figure 5.10 shows different magnetoresistance curves measured at T = 100 K, acquired at different voltage bias. As it is clear, MR intensity is higher for lower voltage bias, and it vanishes when V_{bias} exceeds ∼0.5 V.

5.5 Conclusions

Vertical spin valves have potential applications in memory storage and logic operation. In this chapter we presented a characterization of a spin valve device, using GO sandwiched between two well known ferromagnetic electrodes. We firstly characterized morphologically the GO film deposited on the LSMO bottom electrode, to make sure that the resulting multilayer structure is homogeneous and with no short circuits. Then the device, comprehensive of the top Co electrode, has been electrically characterized in terms of transport mechanisms through the vertical structure, which resulted to be of metallic type between room temperature and 100 K.

A clear inverse MR effect has been detected for temperature $\leq$200 K, with an intensity which increases as the temperature decreases, reaching 2.3% at 100 K.

Finally, the dependence of the intensity of MR effect scales also with the voltage bias, vanishing for V_{bias} $\geq$0.5 V.

These preliminary results show that the LSMO/GO/Co device act as a spin valve, although the intensity of the measured MR is still well below the reported values for other devices having organic semiconductor as Alq_3 as spacing layer [74, 86].

A better control of the interfaces is required, and could lead to improved performance of the device. Yet, such a structure could widen the knowledge about spin relaxation mechanisms in GO and rGO in vertical structures.

Conclusions and Outlook

Thanks to its peculiar properties, easy and cheap methods of production, graphene oxide already spurred intensive research interest and application potentialities. In this thesis, the structure and the electrical properties of reduced graphene oxide thin films were investigated in details, because we believe that a deeper understand is necessary to better tailor and tune the rGO features in order to fabricate improved devices.

In the first part of the thesis, the reduction through thermal annealing was analyzed. The as-deposited GO films were firstly characterized by AFM imaging, showing the possibility to obtain smooth homogeneous thin films with root mean squared roughness of about 2 nm with easy deposition techniques as spin coating.
Micro-Raman spectroscopy was used to reveal structural changes due to the reduction process. The number of sp^2-hybridized domains increases with increasing annealing temperature, in accordance with the Tuinstra-Koenig relation. This indicates that the quality of the rGO film, in terms of defect density, improves with increasing the annealing temperature.

I-V characteristic curves measured before and after the thermal treatment, revealed the establishment of ohmic electrical conduction after the annealing. Moreover, we observed a direct connection between the annealing temperature and the final sheet resistance of the films, which shows that the increasing structural quality of the rGO promotes electrical conductivity between the graphitic domains.

Finally, we were able to monitor directly the thermal reduction process through *in-situ* resistance measurements. These showed that the main changes, represented by a very fast drop of the resistance, occurred in the very first time interval (of the order of few minutes). We ascribed the resistance drop to the evaporation of the residual water trapped among the GO flakes, and the effective release of functional groups. We finally showed that the activation temperature for the thermal reduction is ∼200°C.

The second part of the thesis concerns the charge carrier transport in the rGO thin films. We analyzed the electrical resistivity as a function of temperature and applied magnetic field of rGO films reduced at several intermediate levels.
For annealing at temperatures higher than 700°C, the gain in electrical conductivity is limited, likely for the develop of topological defects introduced by the high temperature of the treatment, affecting the final efficiency of the process.

For all the annealing temperatures, the resistivity curves as a function of the temperature showed a $R = R_0 exp(T_0/T)^{1/3}$ temperature dependence law, down to liquid nitrogen temperatures, characteristic of 2D Mott variable range hopping transport mechanism. The slopes of the linear fit scale with annealing temperature, showing a gain in electrical conductivity consistently with an increasing structural quality of the rGO. At lower temperatures, a crossover to another regime likely occurs.

Resistance as a function of applied magnetic fields showed surprisingly high negative magnetoresistance signals at low temperature, with no visible saturation up to 7 T. We ascribed the measured magnetoresistance to the scattering from magnetic moments originated from defect and vacancies.

We finally studied the dependence of electrical transport in rGO films on the size of the GO flakes, by producing solutions with flakes of ∼200 nm, ∼2μm and ∼20μm average lateral dimensions. XPS analysis showed that at each annealing temperature, the C/O ratio does not depend on the size of the flakes, while we observed clear evidences that charge carrier transport is favored in films composed by larger flakes. Magnetotransport measurements instead, revealed that the lateral dimension of the flakes does not affect the magnetic field dependence, corroborating our conclusion that magnetoresistance has a local origin.

We proposed a phenomenological model to explain the obtained results. Yet, we think that a more complete transport model for such a structure should take into account the contact resistance between the rGO flakes by the introduction of a 3D term in the resistivity law. A systematic study on single flake rGO together with a deeper analysis of transport in films composed by different flake sizes could shed light on the reported deviations from a pure 2D Mott VRH model at low temperature, were the inter-flake resistance may dominates, and also take into account the observed lower resistivity for films composed by larger flakes.

At the end of this work, we presented preliminary results on a GO-based spin valve device in vertical geometry. After AFM morphological characterization of the GO film deposited on a ferromagnetic LSMO electrode, we showed spin valve effect for temperatures $\leq$ 200 K, which increases as the temperature decreases, reaching 2.3% at the lowest temperature T = 100 K.

Vertical spin valve devices with organic semiconductors as Alq_3 and the same ferromagnetic electrodes LSMO and Co already showed much higher magnetoresistance values, up to $\sim$22% at 100 K. We believe that the fabrication of more devices in order to have a wider statistics, and a detailed investigation of the interfaces could improve the performances of our LSMO/GO/Co spin valve.
Besides technological applications, it is also possible, thanks to these spintronic devices, to study the spin relaxation process in GO and rGO in vertical configuration.
Further optimization could come from the possibility given by the GO to be

easily functionalized, and to tune its optoelectronic features by choosing the suitable degree of reduction.

Bibliography

[1] W.S. Hummers and R.E. Offeman. **Preparation of Graphitic Oxide**. *J. Am. Chem. Soc.*, 80(6):1339, 1958.

[2] K.S. Novoselov, V.I. Fal'ko, L. Colombo, P.R. Gellert, M.G. Schwab, and K. Kim. **A roadmap for graphene**. *Nature*, 490:192–200, 2012.

[3] K.S. Novoselov, A.K. Geim, S.V. Morozov, D. Jiang, Y. Zhang, S.V. Dubonos, I.V. Grigorieva, and A.A. Firsov. **Electric Field Effect in Atomically Thin Carbon Films**. *Science*, 306:666, 2004.

[4] B.C. Brodie. **On the atomic weight of graphite**. *Philosophical Transaction R. Society London*, 149:249–59, 1859.

[5] E. Treossi, M. Melucci, A. Liscio, M. Gazzano, P. Samorí, and V. Palermo. **High-contrast visualization of graphene oxide on dyesensitized glass, quartz, and silicon by fluorescence quenching**. *J. Am. Chem. Soc.*, 131(43):15576–7, 2009.

[6] M. Melucci, M. Durso, M. Zambianchi, E. Treossi, Z-Y Xia, I. Manet, G. Giambastiani, L. Ortolani, V. Morandi, F. De Angelis, and V. Palermo. **Graphene-organic hybrids as processable, tunable platforms for pH-dependent photoemission, obtained by a new modular approach**. *J Mater Chem*, 22:1823743, 2012.

[7] M. Melucci, E. Treossi, L. Ortolani, G. Giambastiani, V. Morandi, P. Klar, C. Casiraghi, P. Samorí, and V. Palermo. **Facile covalent**

functionalization of graphene oxide using microwaves: bottom-up development of functional graphitic materials. *J. Mater. Chem.*, 20:905260, 2010.

[8] A. Liscio, G.P. Veronese, E. Treossi, F. Suriano, F. Rossella, V. Bellani, R. Rizzoli, P. Samorí, and V. Palermo. **Charge transport in graphenepolythiophene blends as studied by Kelvin Probe Force Microscopy and transistor characterization**. *J. Mater. Chem.*, 21:292431, 2011.

[9] D.A. Dikin, S. Stankovich, E.J. Zimney, R.D. Piner, G.B.H. Dommett, G. Evmenenko, S.B.T. Nguyen, and R.S. Ruoff. **Preparation and characterization of graphene oxide paper**. *Nature*, 448:45760, 2007.

[10] G. Eda, G. Fanchini, and M. Chhowalla. **Large-area ultrathin films of reduced graphene oxide as a transparent and flexible electronic material**. *Nature Nanotechnology*, 3:2704, 2008.

[11] Y. Zhu, S. Murali, M.D. Stoller, K.J. Ganesh, W. Cai, P.J. Ferreira, A. Pirkle, R.M. Wallace, K.A. Cychosz, M. Thommes, D. Su, E.A. Stach, and R.S. Ruoff. **Carbon-based supercapacitors produced by activation of graphene**. *Science*, 332:153741, 2011.

[12] H-W Liang, X. Zhuang, S. Brüller, X. Feng, and K. Müllen. **Hierarchically porous carbons with optimized nitrogen doping as highly active electrocatalysts for oxygen reduction**. *Nat Commun*, 5:4973, 2014.

[13] S. Han, D. Wu, S. Li, F. Zhang, and X. Feng. **Porous graphene materials for advanced electrochemical energy storage and conversion devices**. *Advanced Materials*, 26(6):849–864, 2014.

[14] Z.Y. Xia, G. Giambastiani, C. Christodoulou, M.V. Nardi, N. Koch, E. Treossi, et al. **Synergic exfoliation of graphene with organic molecules and inorganic ions for the electrochemical production of flexible electrodes**. *ChemPlusChem*, 79(3):43946, 2014.

[15] S. Yang, Y. Sun, L. Chen, Y. Hernandez, X. Feng, and K. Müllen. **Porous iron oxide ribbons grown on graphene for high-performance lithium storage**. *Sci Rep*, 2:427, 2012.

[16] Z-S. Wu, S. Yang, Y. Sun, K. Parvez, X. Feng, and K. Müllen. **3D nitrogen-doped graphene aerogel-supported Fe3O4 nanoparticles as efficient electrocatalysts for the oxygen reduction reaction**. *J. Am. Chem. Soc.*, 134(22):90825, 2012.

[17] K.P. Loh, Q. Bao, G. Eda, and M. Chhowalla. **Graphene oxide as a chemically tunable platform for optical applications**. *Nat Chem*, 2:101524, 2010.

[18] G. Lu, L.E. Ocola, and J. Chen. **Reduced graphene oxide for room temperature gas sensors**. *Nanotechnology*, 20:445502, 2009.

[19] S. Borini, R. White, D. We, M. Astley, S. Haque, E. Spigone, et al. **Ultrafast graphene oxide humidity sensors**. *ACS Nano*, 7(12):1116673, 2013.

[20] S. Prezioso, F. Perrozzi, L. Giancaterini, C. Cantalini, E. Treossi, V. Palermo, et al. **Graphene oxide as a practical solution to high sensitivity gas sensing**. *J Phys Chem C*, 117(20):1068390, 2013.

[21] V.C. Tung, M. J. Allen, Y. Yang, and R.B. Kaner. **High-throughput solution processing of large-scale graphene**. *Nature Nanotechnology*, 4:25–29, 2009.

[22] D.R. Dreyer, S. Park, C.W. Bielawski, and R.S. Ruoff. **The chemistry of graphene oxide**. *Chem.Soc.Rev.*, 39:228–240, 2010.

[23] H. He, J. Klinowski, M. Forster, and A. Lerf. **A new structural model for graphite oxide**. *Chem Phys Lett*, 287(1):536, 1998.

[24] P. Blake, E.W. Hill, A.H. Castro Neto, K.S. Novoselov, D. Jiang, R. Yang, T.J. Booth, and A.K. Geim. **Making graphene visible**. *Applied Physics Letters*, 91(6):063124, 2007.

[25] J. Russier, E. Treossi, A. Scarsi, F. Perrozzi, H. Dumortier, L. Ottaviano, M. Meneghetti, V. Palermo, and A. Bianco. **Evidencing the mask effect of graphene oxide: a comparative study on primary human and murine phagocytic cells**. *Nanoscale*, 5:1123447, 2013.

[26] S. Pei and H.-M. Cheng. **The reduction of graphene oxide**. *Carbon*, 50(9):3210–3228, 2012.

[27] C. Mattevi, G. Eda, S. Agnoli, S. Miller, A.K. Mkhoyan, O. Celik, D. Mastrogiovanni, G. Granozzi, E. Garfunkel, and M. Chhowalla. **Evolution of electrical, chemical, and structural properties of transparent and conducting chemically derived graphene thin films**. *Advanced Functional Materials*, 19(16):2577, 2009.

[28] C. Gómez-Navarro, J.C. Meyer, R.S. Sundaram, A. Chuvilin, S. Kurasch, M. Burghard, K. Kern, and U. Kaiser. **Atomic Structure of Reduced Graphene Oxide**. *Nano Lett.*, 10(4):11441148, 2010.

[29] F. Perrozzi, S. Prezioso, M. Donarelli, F. Bisti, P. De Marco, S. Santucci, M. Nardone, E. Treossi, V. Palermo, and L. Ottaviano. **Use of optical contrast to estimate the degree of reduction of graphene oxide**. *The Journal of Physical Chemistry C*, 117(1):620–625, 2012.

[30] S. Stankovich, D. Dikin, R. Piner, K. Kohlhaas, A. Kleinhammes, Y. Jia, Y. Wu, S.B. Nguyen, and R.S. Ruoff. **Synthesis of graphene-based nanosheets via chemical reduction of exfoliated graphite oxide**. *Carbon*, 45(7):1558–1565, 2007.

[31] J.M. Mativetsky, A. Liscio, E. Treossi, E. Orgiu, A. Zanelli, P. Samorí, and V. Palermo. **Graphene transistors via in situ voltage-induced reduction of graphene-oxide under ambient conditions**. *Journal of the American Chemical Society*, 133(36):14320–14326, 2011.

[32] J.M. Mativetsky, E. Treossi, E. Orgiu, M. Melucci, G.P. Veronese, P. Samorí, and V. Palermo. **Local current mapping and pattern-**

ing of reduced graphene oxide. *Journal of the American Chemical Society*, 132(40):14130–14136, 2010.

[33] Z.Y. Xia, S. Pezzini, E. Treossi, G. Giambastiani, F. Corticelli, V. Morandi, A. Zanelli, V. Bellani, and V. Palermo. **The Exfoliation of Graphene in Liquids by Electrochemical, Chemical, and Sonication-Assisted Techniques: A Nanoscale Study**. *Advanced Functional Materials*, 23(37):4684–4693, 2013.

[34] K. Parvez, Z.-S. Wu, R. Li, X. Liu, R. Graf, X. Feng, and K. Müllen. **Exfoliation of graphite into graphene in aqueous solutions of inorganic salts**. *Journal of the American Chemical Society*, 136(16):6083–6091, 2014.

[35] A.C. Ferrari and J. Robertson. **Interpretation of Raman spectra of disordered and amorphous carbon**. *Phys. Rev. B*, 61(20), 2000.

[36] S. Sahoo, G. Khurana, S.K. Barik, S. Dussan, D. Barrionuevo, and R.S. Katiyar. **In situ raman studies of electrically reduced graphene oxide and its field-emission properties**. *J. Phys. Chem. C*, 117(10):54855491, 2013.

[37] L.M. Malard, M.A. Pimenta, G. Dresselhaus, and M.S. Dresselhaus. **Raman spectroscopy in graphene**. *Phys. Reports*, 473:51–87, 2009.

[38] S. Eigler, C. Dotzer, and A. Hirsch. **Visualization of defect densities in reduced graphene oxide**. *Carbon*, 50(10):36663673, 2012.

[39] T.V. Cuong, V.H. Pham, Q.T. Tran, J.S. Chung, E.W. Shin, J.S. Kim, and E.J. Kim. **Optoelectronic properties of graphene thin films prepared by thermal reduction of graphene oxide**. *Materials Letters*, 64:765–767, 2010.

[40] D. Yang, A. Velamakanni, G. Bozoklu, S. Park, M. Stoller, R.D. Piner, S. Stankovich, I. Jung, D. Field, C. Ventrice, et al. **Chemical analysis of graphene oxide films after heat and chemical treatments by**

X-ray photoelectron and Micro-Raman spectroscopy. *Carbon*, 47(1):145–152, 2009.

[41] F. Tunistra and J.L. Koening. **Raman spectrum of graphite**. *J. Chem. Phys.*, 53:1126, 1970.

[42] N.F. Mott and E.A. Davis. ***Electronic processes in non-crystalline materials***. Oxford University Press, 2012.

[43] C. Gómez-Navarro, R.T. Weitz, A.M. Bittner, M. Scolari, A. Mews, M. Burghard, and K. Kern. **Electric Transport Properties of Individually Reduced Graphene Oxide Sheets**. *Nano Lett.*, 7(10):3499–3503, 2007.

[44] A.B. Kaiser, C. Gómez-Navarro, R.S. Sundaram, M. Burghard, and K. Kern. **Electrical conduction mechanism in chemically derived graphene monolayers**. *Nano letters*, 9(5):1787–1792, 2009.

[45] G. Eda, C. Mattevi, H. Yamaguchi, HK. Kim, and M. Chhowalla. **Insulator to semimetal transition in graphene oxide**. *The Journal of Physical Chemistry C*, 113(35):15768–15771, 2009.

[46] G. Venugopal, K. Krishnamoorthy, R. Mohan, and S.-J. Kim. **An investigation of the electrical transport properties of graphene-oxide thin films**. *Materials Chemistry and Physics*, 132(1):29–33, 2012.

[47] B. Muchharla, TN. Narayanan, K. Balakrishnan, P.M. Ajayan, and S. Talapatra. **Temperature dependent electrical transport of disordered reduced graphene oxide**. *2D Materials*, 1(1):011008, 2014.

[48] S.-W. Wang, HE. Lin, H.-D. Lin, KY. Chen, K.-H. Tu, CW. Chen, J.-Y. Chen, C.-H. Liu, CT. Liang, and YF. Chen. **Transport behavior and negative magnetoresistance in chemically reduced graphene oxide nanofilms**. *Nanotechnology*, 22(33):335701, 2011.

[49] D. Joung and S.I. Khondaker. **Efros-Shklovskii variable-range hopping in reduced graphene oxide sheets of varying carbon sp2 fraction**. *Phys. Rev. B*, 86:235423, 2012.

[50] Y.-B. Zhou, B.-H. Han, Z.-M. Liao, H.-C. Wu, and D.-P. Yu. **From positive to negative magnetoresistance in graphene with increasing disorder**. *Applied Physics Letters*, 98:222502, 2011.

[51] G. Binnig, C.F. Quate, and C. Gerber. **Atomic force microscope**. *Physical review letters*, 56(9):930, 1986.

[52] C.V. Raman and K.S. Krishnan. **A new type of secondary radiation**. *Nature*, 121(3048):501–502, 1928.

[53] C.V. Raman. **A new radiation**. *Indian Journal of physics*, 2:387–398, 1928.

[54] Quantum Design. **PPMS - Hardware Manual**. 2008.

[55] Kulicke and INC. Soffa Industries. **Model 4123 Universal Wedge Bonder Operation Manual**. *Willow Grove, PA, U.S.A.*

[56] L.J. van der PAUW. **A method of measuring specific resistivity and Hall effect of discs of arbitrary shape**. *Philips Res. Rep.*, 13:1–9, 1958.

[57] Keithley. **Low Level Measurements Handbook, 7th Edition**. pages 4–37 – 4–40, 2013.

[58] G.K. Ramesha and S. Sampath. **Electrochemical reduction of oriented graphene oxide films: an in situ Raman spectroelectrochemical study**. *The Journal of Physical Chemistry C*, 113(19):7985–7989, 2009.

[59] K. Erickson, R. Erni, Z. Lee, N. Alem, W. Gannettl, and A. Zettl. **Determination of the local chemical structure of graphene oxide and reduced graphene oxide**. *Advanced Materials*, 22(40):4467–4472, 2010.

[60] C. Punckt, F. Muckel, S. Wolff, I. Aksay, C. Chavarin, G. Bacher, and W. Mertin. **The effect of degree of reduction on the electrical**

properties of functionalized graphene sheets. *Applied Physics Letters*, 102(2):023114, 2013.

[61] I. Jung, D. Dikin, R. Piner, and R. Ruoff. **Tunable electrical conductivity of individual graphene oxide sheets reduced at low temperatures**. *Nano Letters*, 8(12):4283–4287, 2008.

[62] S. Qin, X. Guo, Y. Cao, Z. Ni, and Q. Xu. **Strong ferromagnetism of reduced graphene oxide**. *Carbon*, 78:559–565, 2014.

[63] P.A. Bobbert, T.D. Nguyen, F.W.A. Van Oost, B. Koopmans, and M. Wohlgenannt. **Bipolaron mechanism for organic magnetoresistance**. *Physical Review Letters*, 99(21):216801, 2007.

[64] A. Alexandrov, V.A. Dediu, and V. Kabanov. **Hopping magnetotransport via nonzero orbital momentum states and organic magnetoresistance**. *Physical review letters*, 108(18):186601, 2012.

[65] J.J. Palacios, J. Fernández-Rossier, and L. Brey. **Vacancy-induced magnetism in graphene and graphene ribbons**. *Physical Review B*, 77(19):195428, 2008.

[66] B. Uchoa, V.N. Kotov, N.M.R. Peres, and A.H. Neto. **Localized magnetic states in graphene**. *arXiv preprint arXiv:0802.1711*, 2008.

[67] A.V. Krasheninnikov, P.O. Lehtinen, A.S. Foster, P. Pyykkö, and R.M. Nieminen. **Embedding transition-metal atoms in graphene: structure, bonding, and magnetism**. *Physical review letters*, 102(12):126807, 2009.

[68] M. Ugeda, I. Brihuega, F. Guinea, and J. Gómez-Rodríguez. **Missing atom as a source of carbon magnetism**. *Physical Review Letters*, 104(9):096804, 2010.

[69] Q. Feng, N. Tang, F. Liui, Q. Cao, W. Zheng, W. Ren, X. Wan, and Y. Du. **Obtaining high localized spin magnetic moments by fluorination of reduced graphene oxide**. *ACS nano*, 7(8):6729–6734, 2013.

[70] A. Candini, C. Alvino, W. Wernsdorfer, and M. Affronte. **Hysteresis loops of magnetoconductance in graphene devices**. *Physical Review B*, 83(12):121401, 2011.

[71] G. Khurana, N. Kumar, R.K. Kotnala, T. Nautiyal, and R.S. Katiyar. **Temperature tuned defect induced magnetism in reduced graphene oxide**. *Nanoscale*, 5(8):3346–3351, 2013.

[72] F. Perrozzi, S. Prezioso, and L. Ottaviano. **Graphene oxide: from fundamentals to applications**. *Journal of Physics: Condensed Matter*, 27(1):013002, 2015.

[73] T.D. Nguyen, G. Hukic-Markosian, F. Wang, L. Wojcik, X. Li, E. Ehrenfreund, and Z.V. Vardeny. **Isotope effect in spin response of π-conjugated polymer films and devices**. *Nature materials*, 9(4):345–352, 2010.

[74] Z.H. Xiong, D. Wu, Z.V. Vardeny, and J. Shi. **Giant magnetoresistance in organic spin-valves**. *Nature*, 427(6977):821–824, 2004.

[75] V. Dediu, L.E. Hueso, I. Bergenti, A. Riminucci, F. Borgatti, P. Graziosi, C. Newby, F. Casoli, M.P. De Jong, C. Taliani, and Y. Zhan. **Room-temperature spintronic effects in Alq_3-based hybrid devices**. *Physical Review B*, 78(11):115203, 2008.

[76] V.A. Dediu, L.E. Hueso, I. Bergenti, and C. Taliani. **Spin routes in organic semiconductors**. *Nature materials*, 8(9):707–716, 2009.

[77] S. Mooser, J.F.K. Cooper, K.K. Banger, J. Wunderlich, and H. Sirringhaus. **Spin injection and transport in a solution-processed organic semiconductor at room temperature**. *Physical Review B*, 85(23):235202, 2012.

[78] E. Hill, A.K. Geim, K. Novoselov, F. Schedin, and P. Blake. **Graphene spin valve devices**. *Magnetics, IEEE Transactions on*, 42(10):2694–2696, 2006.

[79] N. Tombros, C. Jozsa, M. Popinciuc, H.T. Jonkman, and B.J. Van Wees. **Electronic spin transport and spin precession in single graphene layers at room temperature**. *Nature*, 448(7153):571–574, 2007.

[80] W. Han and R.K. Kawakami. **Spin relaxation in single-layer and bilayer graphene**. *Physical review letters*, 107(4):047207, 2011.

[81] S. Sanvito. **Molecular spintronics: The rise of spinterface science**. *Nature Physics*, 6(8):562–564, 2010.

[82] S. Wang, Y.J. Shi, L. Lin, B.B. Chen, F.J. Yue, J. Du, H.F. Ding, F.M. Zhang, and D. Wu. **Room-temperature spin valve effects in $La_{0.67}Sr_{0.33}MnO_3/Alq_3/Co$ devices**. *Synthetic Metals*, 161(15):1738–1741, 2011.

[83] B.B. Chen, Y. Zhou, S. Wang, Y.J. Shi, H.F. Ding, and D. Wu. **Giant magnetoresistance enhancement at room-temperature in organic spin valves based on $La_{0.67}Sr_{0.33}MnO_3$ electrodes**. *Applied Physics Letters*, 103(7):072402, 2013.

[84] F. Li, T. Li, and X. Guo. **Vertical Graphene Spin Valves Based on $La_{2/3}Sr_{1/3}MnO_3$ Electrodes**. *ACS applied materials & interfaces*, 6(2):1187–1192, 2014.

[85] C. Barraud, P. Seneor, R. Mattana, S. Fusil, K. Bouzehouane, C. Deranlot, P. Graziosi, L. Hueso, I. Bergenti, V.A. Dediu, F. Petroff, and A. Fert. **Unravelling the role of the interface for spin injection into organic semiconductors**. *Nature Physics*, 6(8):615–620, 2010.

[86] M. Prezioso, A. Riminucci, I. Bergenti, P. Graziosi, D. Brunel, and V.A. Dediu. **Electrically Programmable Magnetoresistance in Multifunctional Organic-Based Spin Valve Devices**. *Advanced Materials*, 23(11):1371–1375, 2011.